Article

Current Biology

Wound repair in plants guided by cell geometry

Graphical abstract

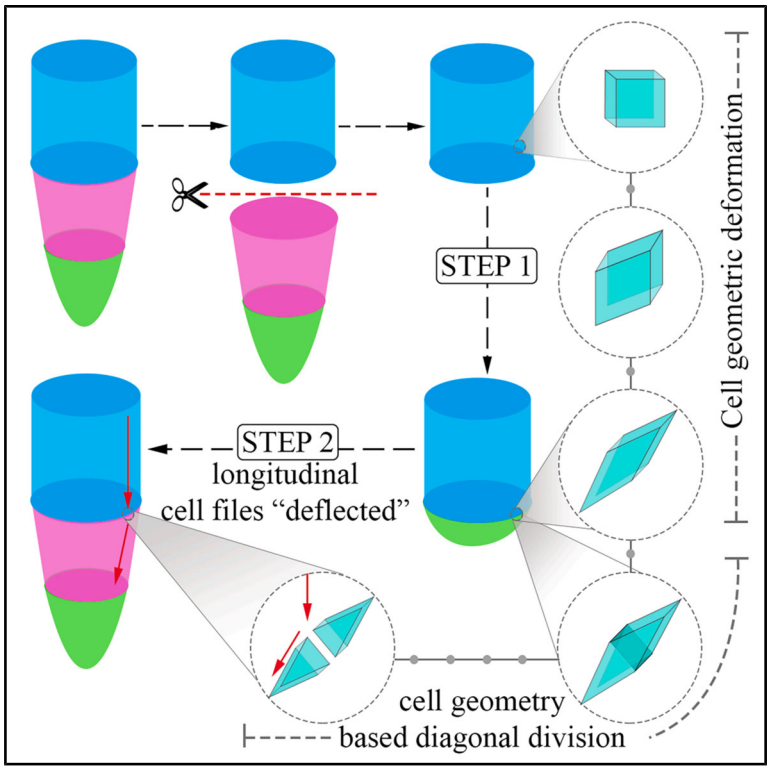

Authors

Mabel Maria Mathew, Jeroen Saccheri, Srijan Das, ..., Ben Scheres, Kirsten Ten Tusscher, Kalika Prasad

Correspondence

mabel.m.mathew@gmail.com (M.M.M.), bandan@iisertvm.ac.in (B.C.), k.h.w.j.tentusscher@uu.nl (K.T.T.), kalika.prasad@iiserpune.ac.in (K.P.)

In brief

Mathew et al. show that growth conflicts reshape cells after injury, forming rhomboidal geometries that trigger diagonal divisions. This reorients cell files to restore tapered morphology. A two-step process—conflict-driven shaping and geometry-guided growth—underlies self-organized morphogenesis in wound repair.

Highlights

- Growth conflicts generate distinct cell shapes following injury
- Cytoskeletons guide cell shaping and atypical diagonal division
- Daughter cells redirect cell files along inclined path to restore root taper
- Local cell geometries guide self-organized morphogenesis in wound repair

Mathew et al., 2025, Current Biology *35*, 3851–3868
August 18, 2025
https://doi.org/10.1016/j.cub.2025.06.072

CellPress

Current Biology

CellPress

Article

Wound repair in plants guided by cell geometry

Mabel Maria Mathew,[1,7,*] Jeroen Saccheri,[2,7] Srijan Das,[1] Kreedika Rajagopalan,[1] Brendan Lane,[4] Sidhardh KA,[5] Richard S. Smith,[4] Viola Willemsen,[6] Monica L. Garcia Gomez,[2,3] Bandan Chakrabortty,[5,*] Ben Scheres,[6] Kirsten Ten Tusscher,[2,3,*] and Kalika Prasad[1,8,*]

[1]Department of Biology, Indian Institute of Science Education and Research (IISER), Pashan, Pune, Maharashtra 411008, India
[2]Theoretical Biology and Bioinformatics, Utrecht University, Utrecht 3584 CH, the Netherlands
[3]Experimental and Computational Plant Development, Utrecht University, Utrecht 3584 CH, the Netherlands
[4]Department of Computational and Systems Biology, John Innes Centre, Norwich Research Park, Norwich NR4 7UH, UK
[5]School of Biology, Indian Institute of Science Education and Research (IISER) Thiruvananthapuram, Vithura, Kerala 695551, India
[6]Laboratory of Molecular Biology, Wageningen University, Droevendaalsesteeg 1, Wageningen 6708 PB, the Netherlands
[7]These authors contributed equally
[8]Lead contact
*Correspondence: mabel.m.mathew@gmail.com (M.M.M.), bandan@iisertvm.ac.in (B.C.), k.h.w.j.tentusscher@uu.nl (K.T.T.), kalika.prasad@iiserpune.ac.in (K.P.)
https://doi.org/10.1016/j.cub.2025.06.072

SUMMARY

In multicellular organisms, the shape of an organ is robust to unpredictable fluctuations. When parts of an organ are removed or damaged, it is often capable of regeneration, restoring its original shape. A central question is how restoration of shape occurs as the collective behavior of individual cells. Here, we use the plant root as an experimental system, surgically removing the tip that contains the organizing center and investigating how it restores its tapered shape. We discover that the transient activation of growth conflicts, which creates specific cell geometries following injury, is vital to this restoration. Using a combination of experimental approaches and computational modeling, we show that non-uniform growth among neighboring cell files generates conflicts, reshaping cuboidal cells into rhomboidal forms. These rhomboidal cells undergo anisotropic growth and establish an atypical diagonal division plane, both of which can be explained by elementary rules of microtubule dynamics. The resulting daughter cells, in turn, guide the growing cell files along an inclined path to restore the tapered morphology. Our findings reveal a two-step process: first, the activation of conflicting growth patterns to generate specific cell shapes, and second, the reorientation of cell division and growth in response to these shapes, recreating the tip-focused cell files that facilitate tapering. This previously unrecognized shape-forming mechanism reveals how local cell geometries, driven by growth conflicts, guide self-organized morphogenesis in plant wound repair.

INTRODUCTION

The diversity of life on Earth stems from the ability of organisms to form distinct structures and shapes. In multicellular organisms, morphogenesis—the process by which tissues and organs acquire their shape—depends on coordinated cellular and tissue-level deformations.[1–7] Studies in both plants and animals have highlighted shared mechanisms, such as bending, buckling, twisting, and turning, which contribute to shaping functional forms.[3,8–19] In animals, these deformations are further complemented by cell migration, slipping, and folding, enabling the generation of intricate structures.[4,20,21] Plants, however, face unique challenges due to their rigid cell walls. Instead of cellular migration, plant morphogenesis relies on local changes in cellular behavior, such as growth rates and anisotropy, to achieve tissue-wide deformation. For example, in *Arabidopsis* sepals, alterations in growth rates and cell shapes can lead to significant changes in sepal morphology.[22]

Roots are critical for below-ground support and nutrient uptake, and their tapering shape and conical tips play a crucial role in soil penetrance.[23–25] The development of roots has been extensively studied, with computational models offering insights into the elongation of embryonic roots,[26] and the auxin-dependent growth and zonation in post-embryonic roots.[27–35] A more recent study suggested that the longitudinal and radial growth in *Arabidopsis* post-embryonic roots is regulated by Brassinosteroid signaling.[36]

Despite the investigations on root development, it is still an open question how the root's characteristic tapering shape gets restored after injury. When the root tip of an *Arabidopsis* seedling is surgically removed (resected) at a limited distance from the stem cell niche (SCN), it regenerates through cell proliferation and repatterning, ultimately restoring its spatial organization and the positioning of all cell types, including the SCN. Importantly, in addition to the restoration of lost cell types and layers, the root also regains its characteristic tapered shape.[37–40] During embryogenesis, the tapering root develops from the basal pole of a single cell. However, after root tip resection in post-embryonic roots, all longitudinal cell files end abruptly, forming a flat surface. These cell files then coordinate their

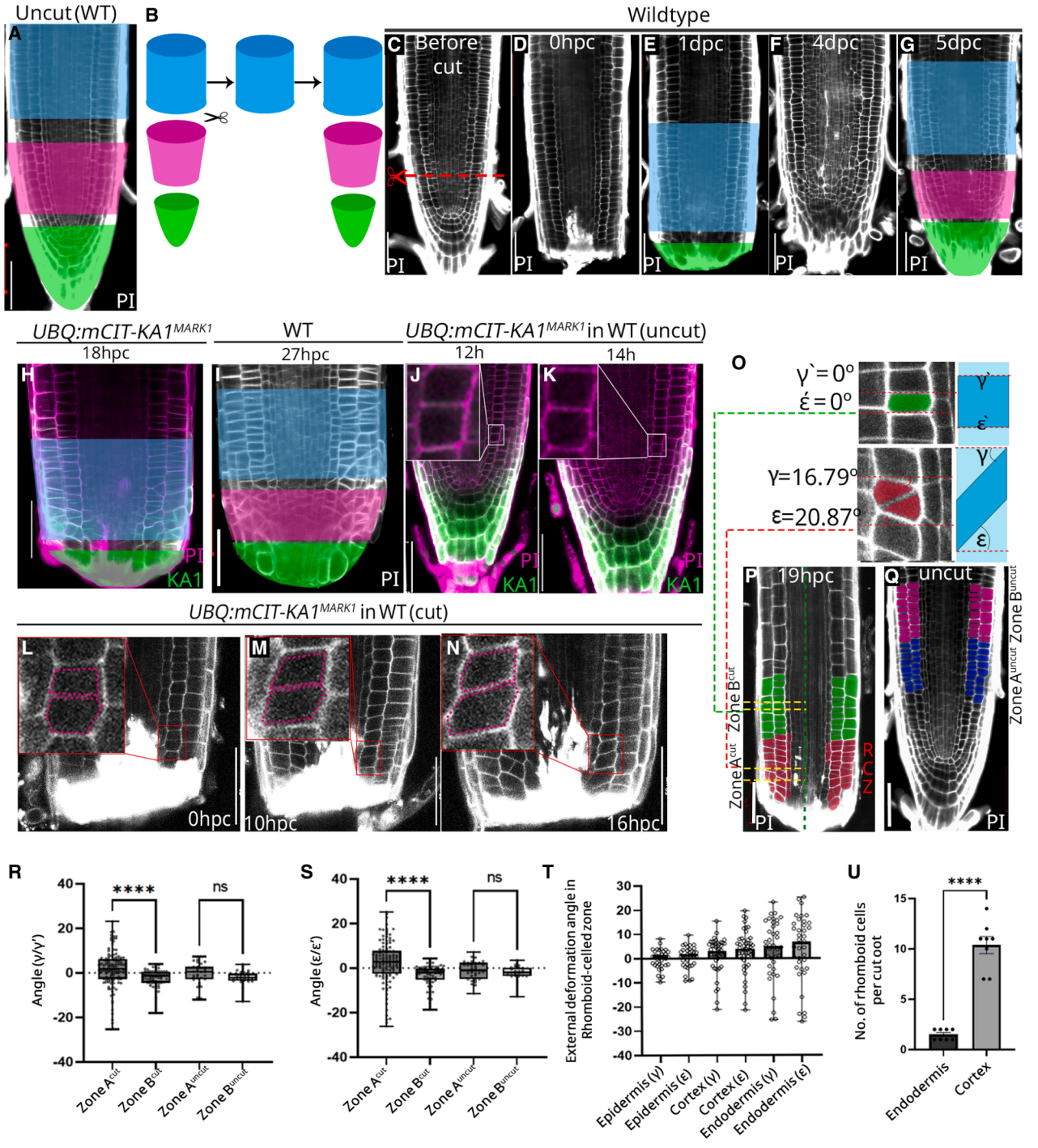

Figure 1. Cells above the cut deform into rhomboid shapes during restoration of root tip

(A) Deconstruction of shape of the *Arabidopsis thaliana* root into three elemental shapes: cylinder (blue), cone frustum (magenta), and ellipsoid hemisphere (green).

(B) Schematic representation of all the elemental shapes during root tip restoration.

(C–G) Confocal-based time-lapse imaging of a representative regenerating root tip post resection in Columbia-0 *Arabidopsis thaliana*. Initially, the root appears like a cylinder (blue) capped by a hemisphere (green) (E), and only later are all the three elemental shapes restored (G). White: propidium iodide (PI) stain. Red dotted line: position of resection.

(H) Representative confocal image of root at initial stage of root tip restoration, where only 2 elemental shapes (cylinder and hemisphere) are restored. Magenta: P1 stain, green: *pUBQ::mCIT-KA1*^{MARK1}.

(I) Representative confocal image of root at the later stage of root tip restoration, where all three elemental shapes are restored.

(legend continued on next page)

growth and organization to restore the root's tapering shape. Previous studies on root tip regeneration have focused on genetic, hormonal, and molecular factors.[39–43] However, cellular mechanisms of shape restoration, specifically cell geometrical inputs behind root tip regeneration, and plant wound repair in general, remain largely unexplored. At least from studies in animals we know that cell geometry changes are crucial during wound healing. For instance, the cells near the wound edge in Drosophila embryos and wing discs undergo deformation, elongating to seal the wound and promote healing.[44–46]

In this study, we investigate how *Arabidopsis thaliana* roots restore their tapered shape following tip excision. We reveal a two-step process guided by cell geometry for restoration of the tapered shape of the root following injury. The first step involves the generation of specific cell geometries through growth conflicts between cell files. The second step uses these specific cell geometries to reorient the longitudinal cell files to facilitate tapering. Disrupting these specific cell geometries impairs tapering and complete restoration. This shape-forming mechanism shows how cell geometry guides self-organized morphogenesis in plant wound repair.

RESULTS

Cell geometry changes during root tip regeneration

The root is a cylindrical organ that gradually tapers toward the tip. We realized that the shape of a root can be broken down into three elementary shapes: a cylinder at the shootward region, i.e., from the transition zone through about three-fourths of the meristem; a cone frustum, where the cylinder gradually narrows in width, i.e., tapers over the remaining quarter of the meristem; and, finally, a cone/hemisphere outlining the columella at the tip (Figure 1A). Studies indicate that roots with only the cylindrical body and conical tip lack efficient soil penetration, highlighting the importance of the tapering.[47] To perform the root tip resection, we took seedlings at 4 days post germination (dpg), when the length of the root meristem was 300–320 μm from the fourth tier of columella. When performing root tip resection (≈210 μm from the fourth tier of columella), we removed the tapered section (cone frustum + hemisphere), leaving the root as a straight, vertical cylinder with a flat end (Figures 1B and 1D). It is known that cells immediately above the cut end undergo rapid cell proliferation to regenerate a new tip.[48] However, successful regeneration requires not only wound closure and proliferation but also the restoration of its original tapered shape. We observed that the resected roots regained all their cell files and original tapered shape by 5 days post cut (dpc) (Figures 1C–1G), which is consistent with prior studies.[39–42] Thus, restoring the original shape involves the reformation of two key shapes: a cone frustum and a hemispherical cap at the tip (Figures 1E and 1G).

A fundamental question arises: what mechanism governs the restoration of tapering? We investigated the cellular mechanism driving the transition of the resected root from a cylinder to a tapered morphology. Toward this, we analyzed the overall shape of the root tip and individual cell behavior above the cut end at 1-h intervals (Figures S1A–S1O). By 18–19 h post cut (hpc), the previously flat cut end of the root began to bulge outward, forming a convex boundary that became more pronounced by 24 hpc (Figures 1E and 1H). As a result, the root first took on the appearance of a cylinder capped by the beginnings of a hemisphere, marking the first phase of shape restoration (Figures 1E and 1H). This was soon followed by the gradual narrowing of the cylindrical part in the rootward direction. As a result, by ≈ 27 hpc, the root took on the appearance of a cylinder, which narrows into a cone frustum capped by a hemisphere. The addition of the cone frustum marks the second phase of shape restoration and thereby the tapering (Figure 1I). During the transition from the flat to tapered morphology, we identified a 10- to 24-hpc developmental window that starts before tapering (Figures S1F–S1J). During this window, 37% of the cells just above the cut end adopt a striking rhomboid-like shape, deviating from the typical cuboidal shape seen in uncut roots at the same location (Figures 1J–1N; Video S1). Notably, such cell geometric deformation primarily occurred in cells present at the time of the cut (0 hpc) (Figures 1L–1N). We found that most rhomboid cells appeared during the 10- to 24-hpc window, although a few continued to appear at later time points. Nevertheless, by 43 hpc, the rhomboid cells were completely undetectable, indicating that the cell geometric deformation was transient (Figures S1K–S1O).

To delve into the spatial distribution of these geometrically distorted cells, we measured the cell's exterior deformation angles (γ, γ', ε, and ε')—the angular changes at the top and bottom outer edges of cells in the meristematic zone—at 19 hpc (The deformations were most prominent at ≈19 hpc) (Figure 1O). These angles

(J and K) Representative confocal time-lapse images of an uncut root. Inset shows the cuboidal cells.
(L–N) Representative confocal time-lapse images of a resected root at 0, 10, and 16 hpc. Inset shows the cell getting deformed into rhomboid shape.
(O) Representative confocal image of a cuboidal and a rhomboid cell in a regenerating root tip, where the $\gamma = 16.79^\circ$ and $\varepsilon = 20.87^\circ$ (left). Schematic representation of external deformation angles in a cuboidal cell (γ', ε') and a rhomboid cell (γ, ε) (right). Red dotted lines: parallel lines perpendicular to the root axis.
(P and Q) Representative live images of a 19-hpc regenerating root tip (left) and an uncut root tip (right) showing zones A^{cut}, B^{cut}, A^{uncut}, and B^{uncut}. Red cells: zone A^{cut} from the cut end, comprising mainly rhomboid cells. Green cells: zone B^{cut} from the cut end, comprising mainly cuboidal cells. Blue cells: zone A^{uncut}, counterpart of A^{cut}, comprising mainly cuboidal cells. Magenta cells: zone B^{uncut}, counterpart of zone B^{cut} cuboidal cells. Yellow dotted lines: parallel lines perpendicular to the root axis (green dotted line). White: PI stain.
(R and S) Graphical representation of the deformation of cells in all four zones, where deformation is significant only in the RCZ (A^{cut}). (Number of roots, $n = 3$; number of cells, x = 117 for RCZ(A^{cut}), 61 for zone B^{cut}, 33 for zone A^{uncut}, and 25 for zone B^{uncut}; Kruskal-Wallis test, $^{****}p < 0.0001$; followed by Dunn's multiple comparisons test, $^{****}p < 0.0001$ for zone A^{cut} vs. zone B^{cut} and $p = 0.1966$ for zone A^{uncut} vs. zone B^{uncut}). Bars: min. and max.
(T) Graph representing external deformation angles of cells within 70 μm from the cut end of 14–19 hpc root tips (RCZ). (Number of roots, $n = 3$; number of cells, x = 35 for epidermis, 46 for cortex, and 38 for endodermis). Bars: min. and max.
(U) Graph showing the number of rhomboid cells in endodermis and cortex of cut root from 10 to 20 hpc (number of roots, $n = 8$; number of cells, x = 12 for endodermis, and x = 83 for cortex; Unpaired two-tailed t test, $^{****}p < 0.0001$). Error bars: SEM. Scale bars: 50 μm.
See also Figure S1 and Video S1.

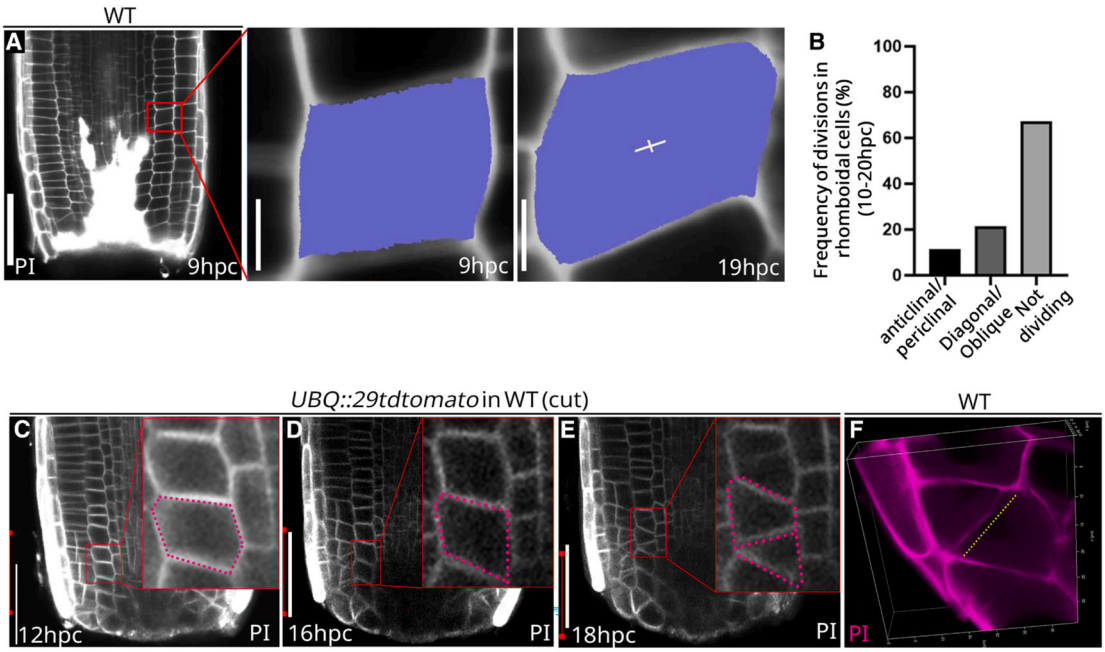

Figure 2. The rhomboid cell grows anisotropically in a tilted direction before undergoing diagonal division

(A) Representative live image of a root at 9 hpc. Inset shows that the principal direction of growth (PDG) of a rhomboidal cell is tilted toward the root apex at 9 hpc (left). The same cell shows anisotropic growth at 19 hpc (right). White line: stretch max, which is "the value of deformation" (stretch ratio) in the maximal direction.

(B) Graph showing the types and frequencies of cell division observed in rhomboid-shaped cells (number of roots, $n = 5$; number of cells, x = 61) in regenerating roots from 10 to 20 hpc.

(C–E) Representative confocal time-lapse images of a resected root at 12, 16, and 18 hpc. Inset shows the anisotropically growing rhomboid cell undergoes division along a near-diagonal plane.

(F) Confocal-based 3D representative image showing near-diagonal division.

Scale bars: 50 μm in (A) and (C–E) and 5 μm in (inset A).

See also Figures S2, S3, and S7.

reflect the extent of cell geometric deformation. In cuboidal cells, the outer deformation angles are typically 0°, and deviations indicate geometric distortion. Rhomboid cells had an increased exterior deformation angle (≈ 5°–20°) (Figures 1O–1T). Interestingly, the highest number of cells undergoing geometric deformation was observed in the cortex (Figure 1U). Notably, the rhomboid cells were absent in intact roots, indicating that they were generated in response to resection (Figures 1O–1S). In resected roots, these deformed cells were found exclusively within a zone located up to 70 μm from the cut end (Figures 1P and 1Q). Thus, this zone—hereafter referred to as the "rhomboid-celled zone" (RCZ)—is both spatially and temporally confined. The cells in RCZ were inclined toward the apex of the regenerating root tip and growing in a tilted direction, exhibiting anisotropic growth (Figure 2A). The orientation of these deformed cells mirrors the slope of the regenerating root (Figure 2A). Remarkably, 21% of the geometrically deformed cells in the RCZ undergo oblique or diagonal divisions, while 12% showed anticlinal or periclinal divisions (Figures 2B–2F). We tracked the cell division plane by live imaging *pUBQ::mCIT-KA1*^{MARK1}[49], which marks newly formed division planes due to its sensitivity to high electronegativity in the newly formed cell walls (Figure S1F). Importantly, no rhomboid cells or diagonal divisions were detected when cuts were made higher (250–300 μm from the fourth tier of the columella; Figures S1P–S1T). As previously shown, regeneration does not occur in high-cut roots and only low-cut roots are competent to regenerate the root tip.[40]

We next asked whether the flexibility of cells in low-cut roots contributed to their geometric deformation to rhomboids. To address this, we constitutively overexpressed PECTIN METHYLESTERASE INHIBITOR 5, which is known to stiffen plant cell walls,[50–52] under a heterologous promoter, *35S::PMEi5* (PMEi5-OE). Rhomboid cells were only rarely observed in the low-cut roots of PMEi5-OE seedlings. Unlike the wild type (WT), even after 24 hpc, the cut end of the low-cut roots of PMEi5-OE remained flat and did not taper (Figures S1Z and S1F′). This suggests that cells in low-cut roots of WT are indeed flexible. Taken together, our data indicate that the formation of rhomboid cells and diagonal divisions is specific to activation of the tapering shape rather than a general response to resection.

Growth conflicts generate the rhomboid cell geometry

We next investigated what triggers the deformation of cells in the RCZ into a rhomboid shape and the first phase of shape restoration, i.e., the formation of a hemisphere-shaped cap at the cut end. Reasoning that cell geometries can be influenced by growth conflicts,[3,53] we hypothesized that growth heterogeneity within

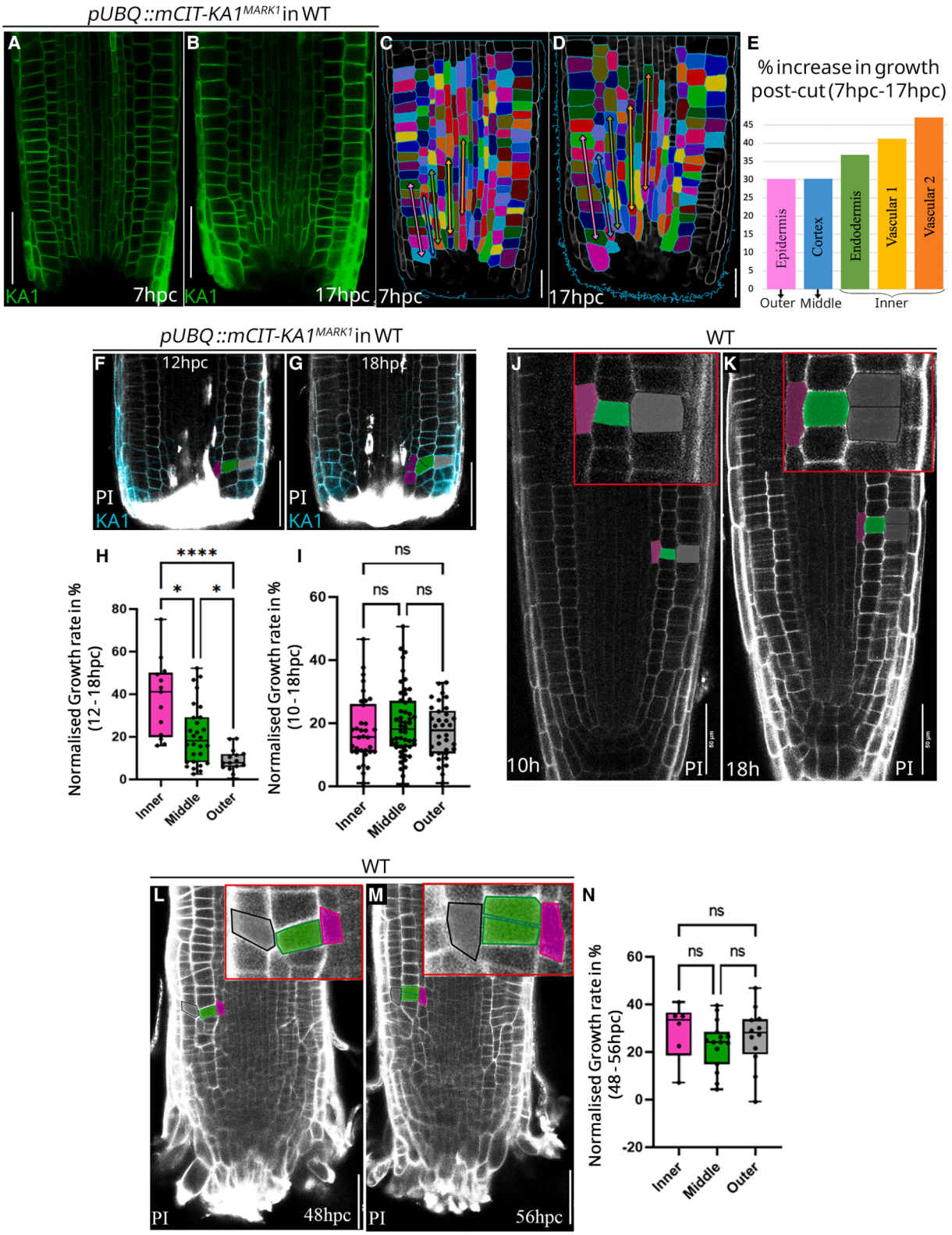

(legend on next page)

the regenerating root could drive the deformation of cells in the RCZ into rhomboids. Because the highest number of rhomboid-shaped cells were observed in the cortex (Figure 1U), we speculated the stele and endodermis to have faster growth and "pull" on the stele-ward side of cortical cells, while the opposite side remains relatively stationary, plausibly due to the slower growth in the epidermal cells.

To test this, we first measured cell growth rates. Because the highest number of rhomboid cells appeared between 10 and 24 hpc, we focused on the period leading up to this critical window to understand what might be triggering their formation. Specifically, we monitored growth in the RCZ of low-cut WT roots from 7 to 17 hpc and compared it with the same region in uncut roots over a similar time span (9–19 h) (Figures 3A–3K and S2A). We observed differences in growth rates among the longitudinal cell files of the regenerating root tip: cells in the stele and endodermis grew faster than those in the cortex, while cells in the epidermis grew more slowly than those in the cortex (Figures 3E, 3H, and S2A). Notably, the rhomboid cells became undetectable once the root achieved noticeable tapering (Figure S1L). This coincided with the time when the stele's growth rate no longer exceeded that of the surrounding cell files (Figures 3L–3N). These data suggest a correlation between the growth rate differences in neighboring cell files and the generation of distinct cell geometries.

To explore whether differences in growth rates between cell files can generate rhomboid cells, we turned to computational modeling. We performed a series of two-dimensional (2D) finite-element simulations of a regenerating root tip using the MorphoMechanX (www.MorphoMechanX.org) framework (Figure 4A; see STAR Methods). In all simulations, all cells within a limited distance from the cut end were simulated to grow, except for the first layer of cells, which corresponds to the dead cells at the cut end. Additionally, we incorporated that epidermal tissue has a 1.5-fold-higher stiffness than the other cell types (Figure 4A). In scenario I, which is the control simulation, all cell layers were assumed to have an equal growth rate (Figure 4B; Video S2, top left). In scenario II, all cell layers were allowed to grow at the same uniform rate, except the stele, which was made to grow faster (Figure 4C; Video S2, top right). In scenario III, the simulation modeled all cell layers to grow uniformly, except for the epidermis, which was made to grow slower (Figure 4D; Video S2, bottom left). Finally, in scenario IV, we mimicked the experimentally observed case, where, among all the cell layers, specified growth in the stele was the fastest and in the epidermis the slowest, with all other cell layers growing at a medium rate (Figure 4E; Video S2, bottom right). The degree of rhomboidness (skew) in cells near the cut end was quantified using the angular approach described in Figure 1O, as well as by measuring the cell axis.

Unlike the control (scenario I), which did not generate any rhomboid cells, all three simulations produced rhomboid cells, suggesting that differential growth between the cell files drives rhomboid cell formation (Figures 4B–4E). However, the one that yielded results most close to experimental observations was scenario IV, where the skewness angle indicating rhomboid-like deformation was most pronounced in the cortex (Figures 4F and 4G). Interestingly, the simulations also showed that the most prominent rotation of cell axes occurred in the cortical cells (Figures S2B and S2D–S2E; Video S3, left). If the dimensions of cortical cells were altered to be shorter and wider, endodermal cells rather than cortical cells displayed the strongest rotation of their cell axes (Figures S2C–S2E; Video S3, right). These findings indicate that, in addition to growth rate differences, the initial aspect ratio of the cell plays a crucial role in generating rhomboid cells, predominantly in the cortex. A side effect of root resection is tissue damage near the cut end, which at times causes the vascular cells near the cut to collapse (Figure 2A). Therefore, it is important to check whether vascular collapse could be an alternative explanation for rhomboid cell formation. To test this, we performed simulations in which vascular cells collapsed both the in presence and absence of growth rate differences (Figures S2F and S2G). Interestingly, we found that vascular collapse alone did not introduce substantial skewing and rotation of cortical cells and, thereby, no rhomboid cells (Figures S2H and S2I; Video S4, left). Meanwhile, when combined with growth rate differences between cell files (higher growth in the stele and slower growth in the epidermis), vascular collapse slightly reduced skewing and enhanced cell axis rotation, suggesting that vascular collapse is not a major factor in

Figure 3. The longitudinal cell files in regenerating roots grow at different rates

(A and B) Representative confocal microscopic image of resected root at 7 and 17 hpc, respectively. Green: *pUBQ::mCIT-KA1*^{MARK1}.

(C and D) Morphograph-X segmentation of the 7 and 17 hpc roots from (A) and (B). The cell files in which longitudinal growth was calculated are shown as lines across the segmented root. Scale bar: 20 μm.

(E) Graphical representation of the longitudinal growth of each cell file in resected root from 7 to 17 hpc, based on growth rate analysis in MGX.

(F and G) Confocal microscopic image of resected root at 12 and 18 h, respectively, where representative inner (magenta), middle (green), and outer (gray) cells taken for growth rate quantification are marked. White: PI stain and Blue: *pUBQ::mCIT-KA1*^{MARK1}.

(H) Graphical representation of growth rate in inner, middle, and outer cells from 12 to 18 hpc; number of roots, $n = 7$; number of cells, x = 13 for inner, 28 for middle, and 15 for outer cell file; Kruskal-Wallis test, $p < 0.0001$, followed by Dunn's multiple comparisons test, $^{*}p = 0.0280$ for inner vs. middle, $^{****}p < 0.0001$ for inner vs. outer, and $^{*}p = 0.0195$ for middle vs. outer.

(I) Graphical representation of the growth of each cell file in uncut root for 8 h (10–18 h). (Number of roots, $n = 4$; number of cells, x = 34 for inner, 52 for middle, and 34 for outer cell file; Kruskal-Wallis test, $p = 0.5486$).

(J and K) Representative confocal microscopic image of uncut root at 10 and 18 h, respectively. Gray: outer (epidermis), green: middle (cortex), magenta: inner (endodermis). White: PI stain.

(L and M) Representative confocal microscopic image of resected root at 48 (L) and 56 hpc (M), respectively. Inset shows representative cells taken for growth rate quantification. Gray: outer (epidermis), green: middle (cortex), magenta: inner (endodermis). White: PI stain.

(N) Graphical representation of the growth of each cell file in cut root from 48 to 56 hpc (number of roots, $n = 2$; number of cells, x = 6 for inner, 15 for middle, and 12 for outer cell file; Kruskal-Wallis test, $p = 0.3916$).Scale bars: 50 μm. Bars: min. and max.

See also Figures S2 and S7 and Videos S3 and S4.

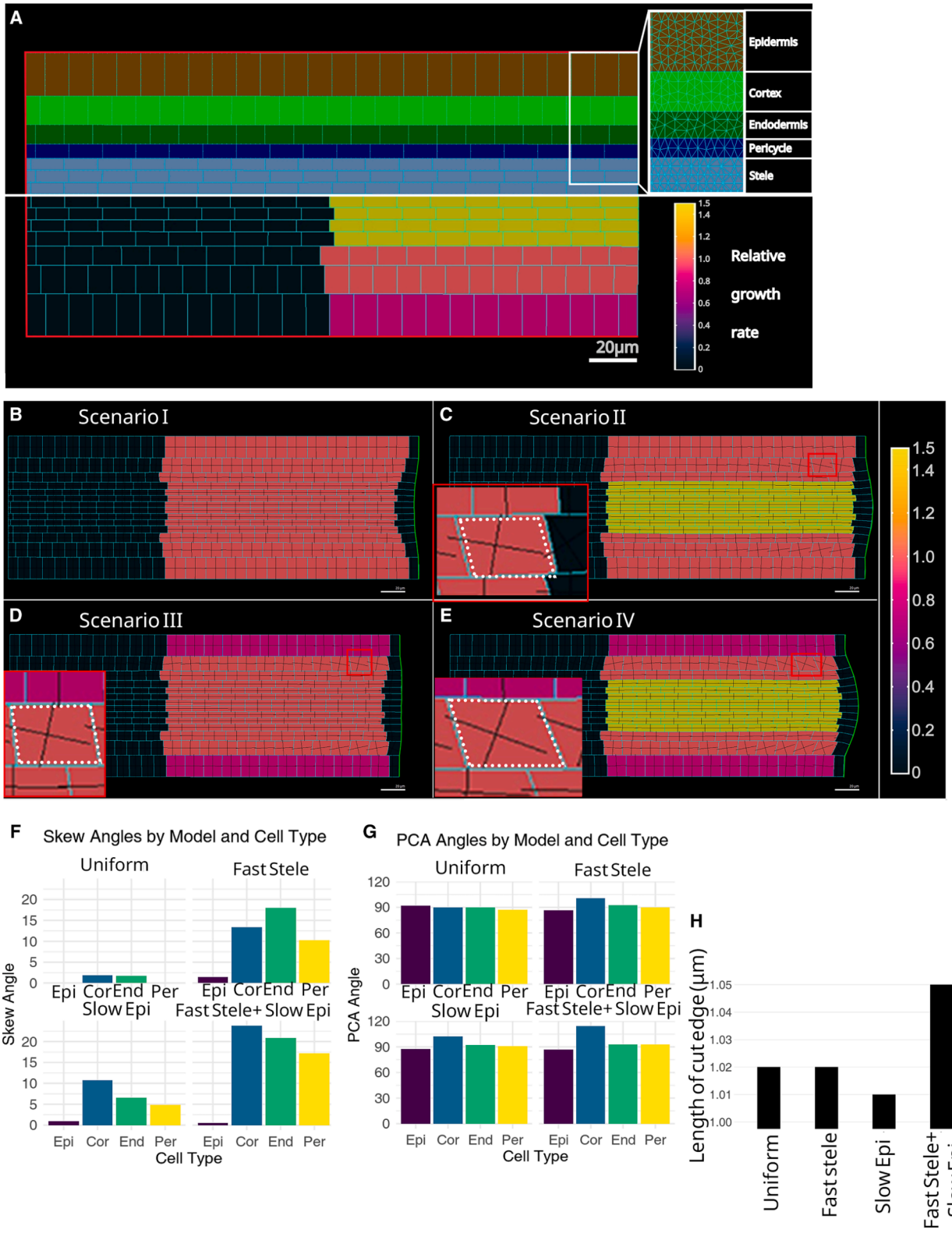

Figure 4. Importance of growth rate differences for inducing cell skewing

(A) The 2D tissue model divides the tissue into cells of distinct cell types (top), which are further refined into triangular finite elements (inset). The finite elements are used in a finite-element method (FEM) simulation that determines the effects of local growth rates on global tissue shape. Growth rates differ between cell types

(legend continued on next page)

root tip shape restoration (Figures S2H and S2I; Video S4, right). Consistent with this, despite the vascular tissue being damaged both in low and high cuts, we observed the preponderance of rhomboid cells only in low-cut roots.

These simulations thus not only identified the cause of rhomboid cell formation but also explain how the initially flat cut edge transformed into a curved, convex boundary, eventually forming a hemisphere-like cap. Theoretically, when inner tissues in a cylindrical structure grow more rapidly than the outer tissues, the base becomes convex rather than remaining flat. To test this hypothesis, the curvature at the cut edge was quantified across all four *in silico* simulations. This was done by measuring the length of the edge spanning from epidermis to epidermis (Figures 4B–4E and 4H). A longer edge length indicated a greater degree of curvature. Although both scenario II and scenario IV resulted in convex edges, the highest edge length—and thus the greatest curvature—was observed in scenario IV, which closely mimicked the experimental conditions (Figures 4C–4E and 4H).

So far, our simulations indicated that differential growth between the cell files drives this geometric deformation. We next examined the necessity of this differential growth experimentally. For this, we used the *woodenleg* (*wol*) mutant, which is known to have reduced vascular initials and decreased cell proliferation in the stele.[54–56] We reasoned that the *wol* mutant, which lacks properly specified vascular initials, would not exhibit the rapid post-resection growth in the stele required to drive the reported cell geometric deformation. It should be noted that the organization of cell files in *wol* remained comparable to WT, although the uncut root meristem in *wol* is shorter. Despite its short meristem and reduced vascular initials, the uncut post-embryonic root meristem of *wol* continued to divide, indicating that the meristem remains capable of growth (Figures S3A–S3F). After root tip resection, we tracked the cell lineages in real time and found that cell proliferation did not cease in *wol* but occurred at a much lower frequency than WT (Figures 5A and S3G). In addition to tracking cell lineages, we also detected cell proliferation in resected *wol* root meristem using 5-ethynyl-2′-deoxyuridine (EdU) staining (Figures S3P–S3S). Unlike WT roots, the resected *wol* mutant roots did not exhibit a significant differential growth rate between inner and outer cell files within the 10- to 18-hpc window (Figures 3F–3H and 5B–5E). As anticipated, unlike the WT, the resected roots of *wol* did not exhibit RCZ, albeit with rare occurrences of 1–2 rhomboid cells (Figure 5F). Additionally, unlike the WT, we did not detect the hemisphere-shaped cap at the base of the cut root that marked the first phase of shape restoration (Figures 5I, 5J, 5N, 5O, S3J, S3K, S3N, and S3O). The root tip regeneration did not progress further in the *wol* mutant (Figures 5G–5Q).

In summary, our theoretical and experimental approaches implicate the differential growth rates between the stele and epidermis in driving the deformation of cells into rhomboids and also suggest a scenario that could trigger the formation of a hemispherical cap at the cut end. These processes together mark the first stage of root shape restoration during root tip regeneration.

Cytoskeleton proteins influence the rhomboid cell shape formation

The cytoskeleton plays a crucial role in establishing and maintaining robust cell shape across kingdoms. In plants, cytoskeleton proteins like actin and cortical microtubules (MTs) regulate the trafficking of cell wall materials and direct anisotropic cell growth. We therefore decided to investigate whether disrupting these components affects rhomboid cell geometry. Given the redundancy in cytoskeletal proteins and the severe growth-retarded phenotype observed in higher-order mutants, we opted for mild pharmacological disruption instead of genetic mutants. Toward this end, we first treated plants with 2,3-Butanedione monoxime (BDM), which inhibits myosin-based actin movement. The roots were exposed to 7 mM BDM immediately after resection (0 hpc to 5 dpc) (Figures 5R–5W). Unlike untreated roots, BDM-treated roots did not develop a prominent RCZ nor display diagonal divisions (Figures 5S, 5V, and S4A), and the number of rhomboid cells was severely reduced (Figure 5X). We cannot rule out the possibility that this impairment in rhomboid cell formation is an indirect consequence of BDM on differential growth between cell files. Therefore, we quantified the growth rate of cells in the BDM-treated resected roots at 12–18 hpc. We did observe growth heterogeneity among the longitudinal cell files (Figure S4C). This suggests that growth heterogeneity is reduced, but not eliminated, in BDM-treated roots (Figures S4C and S4D). Interestingly, the few rhomboid cells that did form lacked anisotropic growth typical of the untreated control (Figures S4B and S4E–S4J). Additionally, the first phase of shape restoration failed, as the cut end did not form a hemispherical cap within 24 hpc, unlike the untreated roots (Figures 5S and 5V). Even by 5 dpc, BDM-treated roots failed to restore their tapering shape, with the cut end remaining flat (Figure 5T, 5W, and 5Y).

The alignment of MTs is crucial for directing cell growth by guiding cellulose microfibril deposition, which, in turn, determines the direction of cell expansion.[57] To test whether MT stability is necessary for rhomboid cell formation, we treated resected roots with 30 μM oryzalin—an MT-destabilizing drug[58]—for 24 h (0 hpc to 1 dpc) (Figures S4K–S4T). This treatment disrupted rhomboid cell shape generation (Figure 5Z). We next quantified the differential growth rates between cell files in

(bottom), and growth only occurs within 130 μm of the tissue's cut end (on the right). To capture the effect of an encapsulating epidermis in 3D, Dirichlet boundary conditions are imposed on all other boundaries of the tissue (red). For further details, see STAR Methods.

(B–E) Simulated tissue state at 19 hpc for different growth rate settings. Tissue state for control conditions with homogeneous growth rates (B). Tissue state for only faster growth in vasculature (C). Tissue state for only slower growth in epidermis (D). Tissue state for faster growth in vasculature and slower growth in epidermis (E).

(F) Skewing angles per tissue type at time 19 hpc for the simulations shown in (B)–(E).

(G) Main axis orientation (PCA angle) per tissue type at time 19 hpc for the simulations shown in (B)–(E).

(H) Tissue edge lengths at time 19 hpc for the simulations shown in (B)–(E). For growth rates applied in the different simulations see STAR Methods.

See also Figure S2 and Videos S2, S3, and S4.

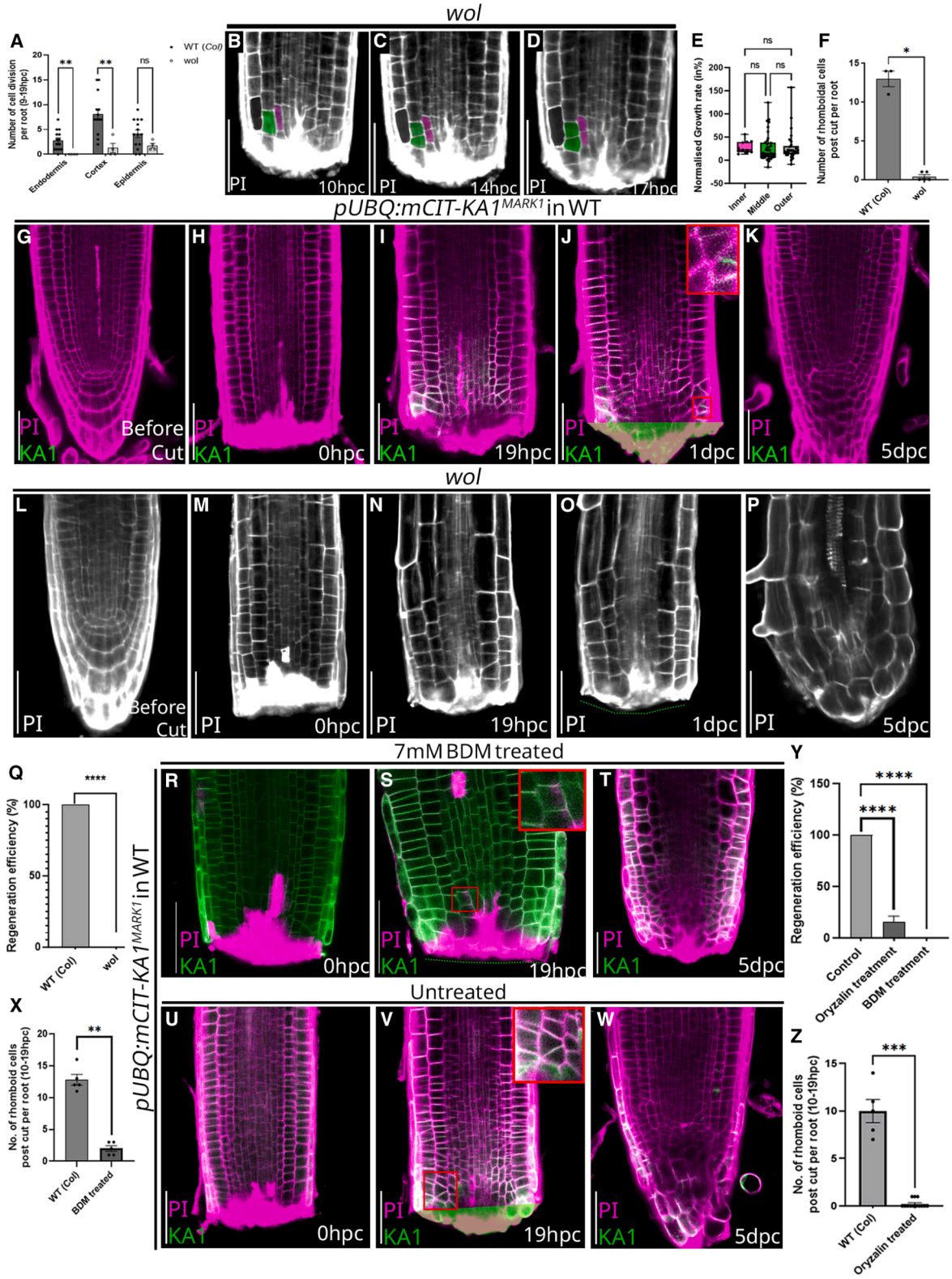

Figure 5. Generation of rhomboid-shaped cells requires growth conflicts

(A) Graphical representation of number of cell divisions in resected *wol* roots compared with WT from 9 to 19 hpc. (Number of roots, $n = 14$ for WT and 4 for *wol*; number of cells, x = 210 for WT, 12 in *wol*; multiple Mann-Whitney tests, $^{*}p = 0.0023$ for endodermis, $^{*}p = 0.0029$ for cortex, and $p = 0.1582$ for epidermis).

(legend continued on next page)

oryzalin-treated roots (12–18 hpc). Similar to BDM treatment, the resected roots showed compromised growth heterogeneity between cell files when treated with oryzalin (Figures S4U and S4V). Although we detected rhomboid cells in oryzalin-treated roots, they were at much lower frequency as compared with untreated control (Figure 5Z). Moreover, these rhomboid cells in the treated roots did not exhibit anisotropic growth and none underwent division along a diagonal plane (Figures S4W–S4C′). Ultimately, the oryzalin-treated roots failed the first phase of shape restoration and did not restore the root tip (Figures 5Y, S4N, S4O, S4S, and S4T). In summary, our results suggest that the cytoskeleton helps shape the rhomboid cells and is important for diagonal divisions of these cells in a regenerating root tip.

Rhomboid cell shape guides the oblique plane of division to restore the U-shaped convergence of longitudinal cell files

Next, we investigated the cellular mechanisms driving the second phase of root tip shape restoration: the tapering. While tracking cell behavior, we consistently observed that rhomboid cells undergo diagonal or oblique divisions, producing daughter cells with a triangular prism-like shape (Figure 6A). An important question is whether this unusual division orientation occurs alongside the formation of rhomboid cells or results from it. Previous models of cell division, such as Errera's Rule, proposes that the cell division occurs along the shortest plane through the centroid. In the case of rhomboid-shaped cells, the longest plane through the centroid corresponds to the major diagonal, connecting the two farthest-apart corners, while the shortest plane is the minor diagonal, connecting the two nearest corners (Figure 6E). So, in theory, it is plausible that the diagonal division in the rhomboid cells is an outcome of the cell shape.

To investigate how rhomboid cell shape may result in diagonal divisions, we performed *in silico* simulations to predict the cell division orientation in rhomboid-shaped cells. These simulations utilized a MT framework, which had previously been applied to model division planes in square-shaped cells.[59] This framework simulates pre-prophase MT dynamics on various cell shapes, incorporating MT properties like nucleation, dynamic instability, and MT interactions[59] (Figure S5A). Additionally, the framework accounts for "edge catastrophes," which refers to the depolymerization of MTs when they cannot cross from one cell face to the adjacent face due to sharp cell edges. These sharp edges arise from smaller angles between adjacent faces, increasing the likelihood of edge catastrophe. To avoid this, MTs form an array away from the sharp edges. This array then organizes into the pre-prophase band (PPB), and its position and orientation determine the division plane's position and orientation (Figure S5B). Under this framework, the simulations reached a steady state, forming a cortical MT array whose orientation was measured by the R vector, which is perpendicular to the cortical MT array.[60] We began by extracting rhomboid cell shapes from microscopic images of regenerating root tips and then simulated MT dynamics within these cells, incorporating both MT-MT and MT-substrate interactions (Figures 6B and 6C). The simulations predicted diagonal MT array orientation, matching the experimentally observed diagonal and near-diagonal division planes (Figures 2F, 6A, and 6D). To validate the predictions made by the *in silico* simulations, we visualized MTs using the GFP-tagged MT-binding domain (*35S::GFP-MBD*) in the root cortical cells using multiphoton microscopy. As predicted by the simulations, we noticed that the cortical MTs in rhomboid cells were oriented diagonally and perpendicular to the direction of cell elongation. Prior to cell division, the MT arrays were observed to bundle along the minor diagonal of the cell, forming a PPB (Figures 6J and 6L), thereby guiding the formation of a new cell plate along the minor diagonal (Figures 6K and 6L). These observations provide experimental validation of the model's predictions.

Subsequently, we investigated the influence of the cell's aspect ratio (aspect ratio [AR] = longest diagonal/shortest diagonal) (Figure 6E) on the likelihood of diagonal division, as a higher AR indicates a greater degree of rhomboidness in theory. To assess this, we first created a cell template with AR = 1, representing a cubic shape (Figure 6F). In this case, MT arrays were randomly oriented, resulting in random division planes

(B–D) Representative confocal time-lapse image of *wol* root tip at 10 (B), 14 (C), and 17 hpc (D). Black represents the outer (epidermal) cell, green represents the middle (cortical) cell, and magenta represents the inner (endodermal) cell. White: PI stain.
(E) Graphical representation of the growth of cells in each cell file in cut root of *wol* from 10 to 18 hpc. (Number of roots, $n = 3$; number of cells, x = 11 for inner, 37 for middle, and 30 for outer cell files; Kruskal-Wallis test, followed by Dunn's multiple comparisons test, $p = 0.3407$ for inner vs. middle, $p = 0.7366$ for inner vs. outer, and $p > 0.999$ for middle vs. outer). Bars: min. and max.
(F) Graphical representation of number of rhomboid cells in *wol* and WT (number of roots, $n = 3$ for WT, 5 for *wol*; number of cells, x = 39 for WT, x = 2; Mann-Whitney U test, $p = 0.0179$).
(G–K) Representative confocal time-lapse image of WT root tip before cut, 0 hpc, 19 hpc, 1 dpc, and 5 dpc. (J) The hemispherical cap at the cut end marked by green contour. Magenta: PI stain and green: *pUBQ::mCIT-KA1*^{MARK1}.
(L–P) Representative confocal time-lapse image of *wol* root tip before cut, 0 hpc, 19 hpc, 1 dpc, and 5 dpc. Note that even at 1 dpc the cut edge remains flat and even by 5 dpc the root tip does not restore the correct tapering. Green dotted line denotes the flat edge at the cut end. White: PI stain.
(Q) Graphical representation of number regenerated roots in WT and *wol* (number of roots, $n = 29$ for WT, $n = 37$ for *wol*; Fisher's test, $^{****}p < 0.0001$). Pharmacological inhibition of cytoskeletal activity impairs rhomboid shape formation and its anisotropic growth.
(R–W) Representative confocal images of BDM-treated roots and corresponding untreated control at 0 hpc, 19 hpc, and 5 dpc. Note that even by 5 dpc, the BDM-treated roots fail to taper and the cut end remains flat (T), unlike the WT (W). Magenta: PI stain and green: *pUBQ::mCIT-KA1*^{MARK1}.
(X) Graphical representation of number of rhomboid cells in WT and BDM-treated roots (number of roots $n = 5$ for untreated and 5 for BDM-treated roots; number of cells, x = 64 for WT, x = 10 for BDM-treated roots; Mann-Whitney U test, $^{**}p = 0.0079$).
(Y) Graphical representation of regeneration frequency in WT, oryzalin-treated regenerating root tips and BDM-treated root tips post resection (number of roots, $n = 46$ for WT, 23 for oryzalin treatment, and 40 for BDM treatment, Fischer's exact test, $^{****}p < 0.0001$ for both).
(Z) Graphical representation of the number of rhomboid cells in WT and oryzalin-treated roots (number of roots, $n = 5$ for untreated and 13 for oryzalin-treated roots; number of cells, x = 50 for WT and 3 for oryzalin treatment; Mann-Whitney test, $^{***}p = 0.0001$). Error bars: SEM. Scale bars: 50 μm.
See also Figures S3 and S4.

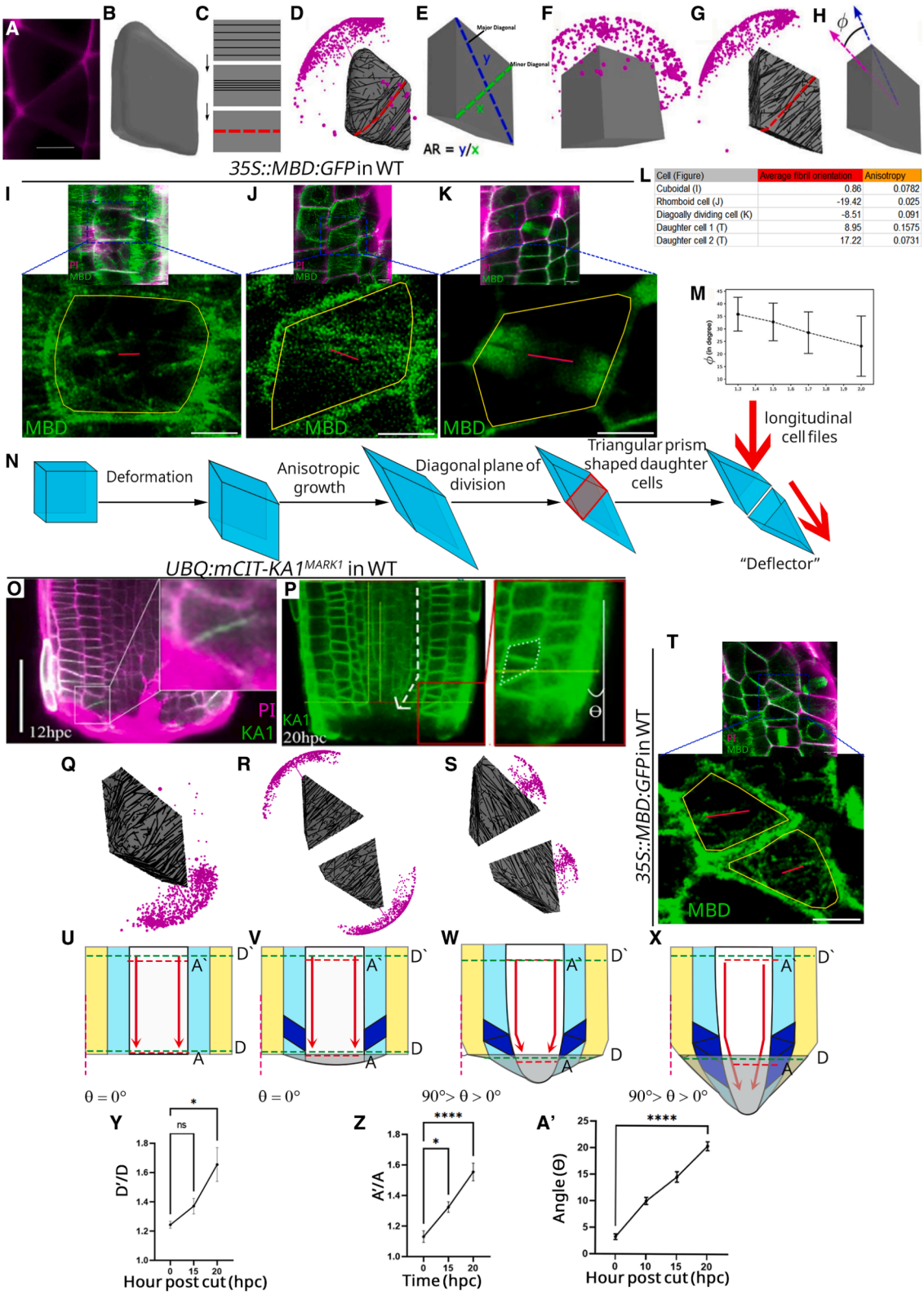

Figure 6. Rhomboid cell geometry guides the oblique plane of division to restore shape of the root tip

(A) Representative confocal-based 3D reconstitution of a rhomboid cell with diagonal division. Scale bar: 5μm.

(B) Representative rhomboid cell (3D reconstruction by merging the daughter cell pair in MGX).

(legend continued on next page)

(Figure 6F). When the AR increased to 1.66, matching experimentally observed rhomboid cells, MT arrays aligned diagonally, indicating a preferred diagonal plane of division (Figure 6G and S5C). Next, we quantified the precision of the predicted diagonal division. To do this, the angle (ϕ) between the cell's principal (longest) axis and the R vector was measured (Figure 6H). This angle (ϕ) represents the deviation of the division orientation from the predicted diagonal division (Figure 6H). Simulations showed that as the AR increased, ϕ decreased, indicating that the division orientation became more strongly biased toward diagonal division (Figure 6M). It is interesting to note that the predicted plane is very close to the shortest axis. Our simulation predicted the natural variation in the predicted division plane, where the division plane can have a small deviation from the shortest axis. Moreover, the precision of the oblique division plot indicates that the division prediction becomes closer to the shortest axis with a higher value of cell rhomboidness, i.e., higher cell AR.

(C) Schematic representation of cell division orientation via MT array. MTs, through dynamic interactions, form an ordered array (top). The MT array then forms a ring-like structure called pre-prophase band (PPB, middle). The position and orientation of the PPB determine the corresponding position and orientation of the division plane (bottom).
(D) Simulation of MT dynamics on the surface of experimentally obtained rhomboidal cell shape showing oblique orientation of MT array vector tips R (magenta dots). The arrow vector (magenta arrow) represents the mean orientation of the associated MT array.
(E) The cell aspect ratio is defined as the ratio of the magnitude of the major axis (*y* dimension) and minor axis (*x* dimension) of the cell.
(F) Simulation of MT dynamics on a cuboidal cell shape, i.e., with AR = 1, showing random orientation of MT array vector tips.
(G) Simulation of MT dynamics on an experimentally equivalent idealized rhomboid cell shape showing oblique orientation of MT array vector tips.
(H) Schematic representation of the deviation angle of the division plane from the oblique division (Φ), the angle between R (magenta arrow), and the principal axis (blue arrow) of the rhomboid cell shape.
(I) Representative multiphoton-based live image showing the orientation of cortical microtubules in a cuboid-shaped cortical cell immediately post resection. Inset shows a single cuboid cell with its principal microtubule orientation marked by the red line. Green: *35S::GFP:MBD*, magenta: PI. Scale bar: 5 μm.
(J) Representative multiphoton-based live image showing the anisotropic orientation of cortical microtubules in a rhomboid-shaped cortical cell in a regenerating root. Inset shows a single rhomboid cell with its principal microtubule orientation marked by the red line. Green: *35S::GFP:MBD*, magenta: PI. Scale bar: 5 μm.
(K) Representative multiphoton-based live image of a diagonally dividing rhomboid cell, showing the arrangement of microtubules near the newly forming cell plate that guides the formation of a diagonal division plane. Inset shows enlarged image of a single cell with principal microtubule orientation marked by the red line. Green: *35S::GFP:MBD*, magenta: PI. Scale bar: 5μm.
(L) Average fibril orientation and anisotropy of the cells shown in (I)–(K) and (T).
(M) Simulated values of the deviation angle as a function of the cell AR, simulations were performed on idealized rhomboid cell shapes with fixed cell thickness, which we set to the experimentally obtained average cell thickness (z = 1). The green dot represents when simulations were performed on the experimental rhomboidal cell. For each cell shape, simulations were performed for 1,000 independent configurations of stochastic MT dynamics under the same MT-dynamical parameters. Detailed simulation parameterization is described in the supplemental information.
(N) Schematic representation theorizing the stages of a deformed cell. The cuboidal cell first deforms into a rhomboid, which then grows anisotropically and undergoes diagonal division to produce a pair of daughter cells shaped like triangular prisms. The daughter cells then proceed to act like "deflectors" to prompt the vertically growing longitudinal cell files to take a subtle turn and continue along an inclined trajectory.
(O) Representative confocal-based live image of a resected root at 12 hpc. Inset shows a rhomboid cell with diagonal division. Magenta: PI stain, green: *pUBQ::mCIT-KA1*^{MARK1}. Scale bar: 50 μm.
(P) Representative confocal-based live image of a resected root at 20 hpc. Inset shows the initiation of tapering (depicted by $90^\circ < \theta > 0^\circ$), which spatially coincides with that of a rhomboid cell with diagonal division. White dashed arrow indicates the deflection of the longitudinal cell files. White dotted line shows a rhomboid cell with diagonal division. Green: *pUBQ::mCIT-KA1*^{MARK1}. Scale bar: 50 μm.
(Q) Simulation of MT dynamics predicts that rhomboid cells undergo anisotropic growth prior to oblique/diagonal division. It should be noted that the cell grows in a direction perpendicular to the MT array.
(R and S) Simulation of MT dynamics on the two triangular prism-shaped daughter cells post diagonal division predicts a 70% probability of tilted growth (R) and 30% probability of transverse growth (S).
(T) Representative multiphoton image of prism-shaped daughter cells resulting from a diagonally divided rhomboid cell. The cortical microtubules of these cells are oriented in the direction promoting a tilted growth. Inset shows prism-shaped daughter cells, with their principal microtubule orientation marked by the red line. Green: *35S::GFP:MBD*, magenta: PI. Scale bar: 5 μm.
(U–X) This schematic representation depicts the progression of shape recovery during root tip regeneration, focusing on how rhomboid cell deformation and alignment contribute to the tapering process. Immediately after the root tip is resected, the cut end remains flat. θ refers to the angle of tapering or deviation of the root tip during regeneration. Initially, the regenerating root tip is straight, with no tapering ($\theta = 0^\circ$), meaning that the cells align vertically (U). Yellow represents the epidermis (outer cell file), blue represents the cortex/endodermis (middle cell file), and white indicates the stele/pericycle (inner cell file). The red arrow shows the growth direction of the inner cell file. As the inner cell files grow faster, cells in the middle cell file undergo geometric deformation into a rhomboid shape (V). Gray shows the regenerated portion below the cut end. The rhomboid cells (dark blue) then undergo diagonal divisions, producing daughter cells that are inclined toward the slope of the root apex rather than aligned vertically. This causes the inner cell files to deviate from their original vertical growth axis and take a subtle turn. As this occurs, θ increases, indicating that the tip is no longer straight but is sloped (PI) (W). Tapering becomes more pronounced as additional cells deform into the rhomboid shape and continue undergoing diagonal divisions (X). Red dotted vertical lines indicate the original growth axis of the root, while green dotted horizontal lines denote the diameter of the root, spanning from epidermis to epidermis. Red dotted horizontal lines mark the diameter of the stele.
(Y) Graph depicting D′/D, the ratio of the root's diameter at the transition zone (D′) to its diameter at the position of diagonal division near the cut end (D) from 0 to 20 hpc (number of roots, $n = 12$; Kruskal-Wallis test, $^*p = 0.0193$, followed by Dunn's multiple comparisons test, $p = 0.5389$ for 0 vs. 15 hpc and $^*p = 0.0105$ for 0 vs. 20 hpc).
(Z) Graph depicting ratio of the stele diameter at the transition zone (A′) to that at the position of diagonal division near the cut end (A) from 0 to 20 hpc (number of roots, $n = 9$; Kruskal-Wallis test, $^{****}p < 0.0001$, followed by Dunn's multiple comparisons test, $^*p = 0.0350$ for 0 vs. 15 hpc and $^{****}p < 0.0001$ for 0 vs. 20 hpc).
(A′) Graph depicting the angle of tapering (θ), which denotes the degree of deviation of the regenerating root from vertical (straight) alignment from 0 to 20 hpc (number of roots, $n = 8$; paired t test, $^{****}p < 0.0001$). Error bars: SEM.
See also Figure S5.

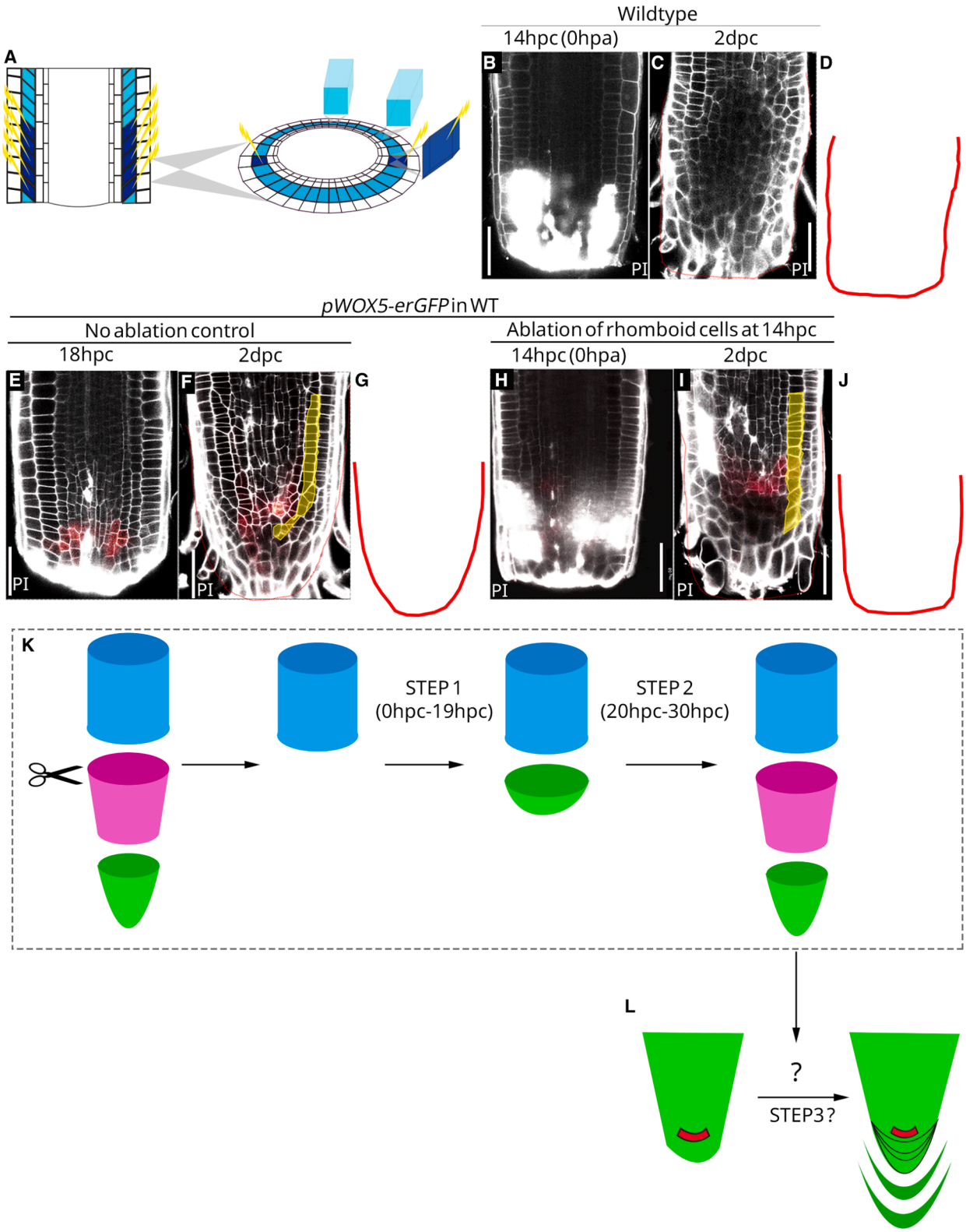

Figure 7. Rhomboid cells are necessary for initiating the tapering during root tip restoration

(A) Schematic representation of rhomboid cell ablation in regenerating root tips. Left: longitudinal section (LS) showing ablation of five rhomboid cells on each side of the stele. Right: cross section (CS) showing ablation of two rhomboid cells on opposite sides of the stele. Light blue: cortical cells. Dark blue: ablated cells.

(legend continued on next page)

Having established that rhomboid cell shapes lead to diagonal divisions, where one daughter cell is displaced outward and the other toward the tip, we speculated that these daughter cells act as a "deflector," redirecting vertically growing longitudinal cell files and guiding them onto an inclined trajectory (Figures 6N and 6O). Consistent with this hypothesis, we observed that by ≈ 20 hpc, the longitudinal cell files encountering these daughter cells deviate from their straight vertical path and take a subtle turn onto an inclined trajectory (Figure 6P). Moreover, we observed that the prism-shaped daughter cells resulting from the diagonal divisions exhibited anisotropic MT orientation (Figure 6L). The MTs were mostly parallel to the newly formed cell wall (Figure 6T). In line with this, our simulations predicted that most of these triangular prism-shaped daughter cells grow anisotropically, where the tip of the prism elongates perpendicular to the MT orientation. Such anisotropic growth of the tilted daughter cells further accentuates their role as deflectors (Figures 6Q–6T). The deviation in the longitudinal cell files, which most likely is an outcome of these deflectors, is critical for the narrowing of the cylindrical root into a cone frustum shape, a key step in restoring the tapering shape of the root tip.

To investigate whether the rhomboid cells and its daughters indeed cause the deflection of longitudinal cells files, we analyzed the relationship between diagonal divisions in rhomboid cells and root tapering. The beginnings of tapering were first observed at ≈ 20 hpc, which is 8 h after the first appearance of diagonal division (Figures 6O and 6P). The initiation of this tapering coincided spatially with the location of the triangular prism-shaped daughter cells (Figures 6P and 6U–6X). Quantitatively, this was captured by the D′/D ratio, which represented the root's diameter at the transition zone (D′) relative to the diameter near the cut end where diagonal divisions occurred (D). The D′/D ratio increased from 1.243 ± 0.083 at 0 hpc to 1.655 ± 0.040 at 20 hpc, indicating root narrowing (Figures 6Y and S5D–S5G). A similar pattern was observed in the stele, where the A′/A ratio—the stele diameter at the transition zone (A′) relative to its diameter near the cut end (A)—increased from 1.131 ± 0.11 at 0 hpc to 1.554 ± 0.174 at 20 hpc (Figures 6Z and S5D–S5G).

These structural changes aligned with an increase in the angle of tapering (θ), which measured the deviation of the regenerating root from vertical growth. Initially, at 0 hpc, $\theta \approx 3^{\circ}$, indicating near-vertical alignment (Figures 6U–6W and 6A′). By 18–20 hpc, θ increased to $\approx 20^{\circ}$, marking the onset of tapering (Figures 6X, 6A′, and S5H–S5K). It should be noted that, at 20 hpc, θ was measured at a position that coincided with the spatial location of the diagonal divisions. Together, these findings demonstrated longitudinal cell files deviated from their original vertical path and continued along an inclined trajectory. This deviation coincided precisely with the spatial position of the diagonally divided cells, underscoring their critical role in driving root tapering.

In summary, we show that the second phase of shape restoration is driven by the diagonal divisions of rhomboid cells, which serve as deflectors, redirecting vertically growing longitudinal cell files onto an inclined trajectory. This deviation is crucial for the narrowing of the root's diameter, initiating the tapering and thereby restoring all the three elemental shapes of the root: cylinder, cone frustum, and a hemisphere.

Rhomboid-shaped cells are essential to activate tapering in regenerating root tips

To further cement our hypothesis that rhomboid-shaped cells are essential for tapering during root regeneration, we ablated rhomboid cells from the RCZ at 12–16 hpc using targeted laser ablation (Figures 7A–7J). Because most of the rhomboid cells were from the cortex, we focused the ablation on cortical cells. It is important to note that we did not ablate all rhomboid cells in the RCZ. Given the cylindrical, three-dimensional (3D) structure of the root, the rhomboid cells are arranged in a circular pattern around the stele. Due to technical limitations in accessing all cells at high resolution and to avoid excessive damage that could impair regeneration, we ablated only 10–15 clearly resolved cells in the middle plane (hereafter referred to as ablated roots) (Figure 7A). Consequently, by 2 dpc, the longitudinally growing cell files in ablated roots remained vertical, whereas those in unablated control roots deflected into an inclined axis (Figures 7F–7J). More importantly, while control roots with intact rhomboid cells achieved robust tapering by 2 dpc, the ablated roots with their rhomboid cells removed did not taper; rather, the cut end remained flat at this stage (Figures 7C,7D, 7F, 7G, 7I, and 7J). As a control for the potential effects of targeted cell ablation, including local heating, on root tapering, we ablated 10–15 non-rhomboid cells at 14 hpc from the epidermis. Strikingly, we observed that these roots with intact rhomboid cells displayed tapering by 2 dpc, similar to unablated roots (Figures S6D–S6F). Furthermore, to address the possibility of altered growth heterogeneity after ablation, we measured the growth rate of cells between 14 and 24 hpc, following the ablation of rhomboid cells at 14 hpc. Notably, we found that the growth heterogeneity between longitudinal cell files remained similar to unablated roots (Figures S6G and S6H). This shows that the impaired tapering of the resected root is not a general consequence of ablation but a result of the removal of rhomboid cells.

(B–J) Ablation of rhomboid cells. Laser-targeted removal of 10–16 rhomboid cells at 16 hpc impairs tapering initiation in resected root tips (B–D and H–J). By 2 dpc, the regenerating root tip without rhomboid cells remains flat (C,D, I, and J) compared with the tapered shape in control roots (F and G), where rhomboid cells remain intact. Expression of the root stem cell regulator, WOX5, remains comparable between the ablated roots (I) and the control (F). Note that the cortical cell file (yellow) takes a turn in (F) but not in (I). Red dotted/solid lines: contours of root tips at 2 dpc. White: PI stain.

(K) Schematic representation depicting the two steps of root tip restoration. Upon resection, the tapering part of the root is removed, leaving behind only a cylinder-shaped part. By 19 hpc, the boundary at the cut end bulges in a convex fashion such that the root appears like a cylinder capped by a hemisphere. This marks step 1. After 20 hpc, the root begins to taper, such that the root appears like a cylinder that narrows into a cone frustum capped by a hemisphere. This marks step 2.

(L) Schematic depiction the shedding of the first few regenerated root cap layers.

Scale bars: 50 μm.

See also Figure S6.

Interestingly, despite the lack of tapering at 2 dpc, the expression pattern of the root stem cell regulator, WUSCHEL-RELATED HOMEOBOX 5 (WOX5), was unaffected in the ablated roots and similar to that of control roots (Figures 7E–7J). This indicates that the role of rhomboid cells in initiating root tapering is independent of stem cell positioning and activity. We observed that the cell proliferation and expansion in the ablated roots did not cease. The new rhomboid cells replaced the ablated ones, thereby activating tapering by 3 dpc, after a delay of ~24 h (Figure S6I and S6J). Thus, the removal of a subset of the rhomboid cells significantly delayed the activation of tapering. In summary, the data from laser ablation demonstrate that the cut end of the root after resection remains flat in the absence of rhomboid cells and regains its tapering shape only after the reappearance of rhomboid cells.

Thus, our findings indicate that rhomboid cell shape activates the tapering in regenerating root tips.

DISCUSSION

Our study reveals how the interaction between growth rate differences, cell shape, and division orientation drives organ shape restoration. Using *Arabidopsis thaliana* root tip regeneration as a model, we investigated the factors that restore the tapered shape of regenerating roots. Based on the experimental and computational data, we suggest a two-step model (Figure 7K) that outlines the cellular and tissue-wide events involved in this process. In step 1 (10–19 hpc), faster growth in the stele and slower growth in the epidermis deforms cortical cells near the cut end into rhomboid shapes, which then undergo anisotropic growth (Figures 6Q and 6T). Meanwhile, the unequal growth between cell files creates a curved boundary at the cut end, transforming the root from a cylinder with a flat base to one capped by a hemisphere. In step 2 (20–30 hpc), diagonal cell divisions in the rhomboid cells generate triangular prism-shaped daughter cells, where one daughter cell is displaced outward and the other toward the tip, acting as deflectors to redirect the vertical longitudinal cell files into inclined trajectories (Figures 6N and 6Q–6T). This inclination narrows the root's diameter, initiates tapering, and ultimately restores the root's three key shapes—cylinder, cone frustum, and hemisphere (Figures 6U–6X and 7K). As a next step, the true U-shaped, continuous form at the tip of the root is likely achieved by the reactivation of the SCN and the renewed ability to shed root cap cells. The newly formed SCN produces contiguous columella cell layers, which are pushed distally in the process (Figure 7L). Shedding the first few regenerated root cap layers likely facilitates the continuity of subsequent layers, effectively creating again a closed U-shaped system.

Interestingly, much like *Arabidopsis*, the closely related *Brassica juncea* also displayed cell geometric deformation of cells to rhomboids and a diagonal plane of division during root tip regeneration (Figures S7C and S7D). Thus, it is tempting to speculate that cell-geometry-guided wound repair is conserved across plant species. Although our analysis focused on the influence of cell geometry on division orientation, we do not rule out the contribution of mechanical stress. Errera's Rule has also been interpreted to mean that the shortest axis of the cell corresponds to the direction of maximal tensile stress.[61] Although we did not directly measure mechanical stress in this study, the observed MT alignment and diagonal divisions correlate with such stress-aligned behavior, suggesting that mechanical cues may act in concert with cell geometry to guide the diagonal plane of division.

It makes one wonder what causes the stele in resected roots to grow faster than the remaining cell files. Injury-induced faster proliferation observed in the stele has been previously reported to be between 10 and 18 hpc,[62] suggesting that factors triggering this rapid growth are activated before this period. One key player in this process appears to be auxin, which surges at the cut end by 6 hpc due to both local biosynthesis and accumulation.[63,64] This excess of auxin at the cut end likely needs to be stabilized. In uncut roots, an auxin reflux loop at the SCN at the distal tip stabilizes auxin levels.[63] However, with root tip resection, the distal tip and SCN are removed, disrupting the reflux loop and destabilizing auxin levels. To restore stability, we propose that a new SCN must form distally. Consistent with this notion, transient inhibition of auxin signaling abrogated the differential growth between longitudinal cell files in regenerating root tips and left the cut end flat (Figures S7F–S7S). During a short 6- to 12-hpc window, auxin and cytokinin briefly overlap in the stele, marking the site for the new SCN.[39] Based on this, we speculate that the dynamics of auxin and cytokinin likely trigger the faster growth in the stele and help to position the new SCN distally. Could the pull from the fast-growing inner (stele) cell files alone explain the formation and maintenance of rhomboid-shaped cells? Although currently speculative, it is tempting to consider that this force might work in tandem with centripetal constriction from the outer (epidermis) cell files and facilitate the anisotropic inward growth of these rhomboid cells.

Our efforts to uncover the genetic basis of the observed geometric deformation are limited by certain constraints. For instance, many genetically engineered backgrounds that manipulate cell wall properties makes it difficult to decouple its effects on cell shape from its effect on cell growth. Changes in cell wall remodeling generally affect the overall growth of regenerating cells. Additionally, several mutants related to cell shape or directional growth in different genetic backgrounds resulted in loss of regeneration, with cells seldom dividing or expanding. A golden standard for such a mutant would allow cells at the cut site to continue dividing and expanding but fail to align their growth anisotropically in response to mechanical stress, and this, to our knowledge, is not available yet. This would create the ability to disrupt the directionality of the cells by impairing the MT or cellulose microfibril alignment in response to stress while preserving overall cell division and expansion after root tip resection. Notwithstanding these challenges for future in-depth research, our study reveals that coordinated changes in local cell geometry, division axes, and growth reorientation guide tapering of an organ and thereby restore organ shape after damage without the ability to recruit cells from elsewhere as used in animal wound repair.

RESOURCE AVAILABILITY

Lead contact

Requests for further information should be directed to, and will be fulfilled by, the lead contact, Kalika Prasad (kalika.prasad@iiserpune.ac.in).

Materials availability

This study did not generate any new materials.

Data and code availability

- Raw data from main Figures 1, 2, 3, 4, 5, 6, 7, and Figures S1–S7 have been deposited at Mendeley and are publicly available as of the date of publication at Mendeley data: https://data.mendeley.com/preview/vyyvby3hv2?a=f6e125e8-1660-4694-b16f-209f6d5fc43
- The growth simulations are run with an in-house-built plugin for MorphoMechanX (https://morphographx.org/morphomechanx/) are publicly available as of the date of publication at Zenodo: https://doi.org/10.5281/zenodo.15698229 (or) Github: https://github.com/kirstentt/regeneration_rhomboids.
- Any additional information required to reanalyze the data reported in this paper is available from the lead contact upon request.

ACKNOWLEDGMENTS

We would like to thank IISER Pune for its infrastructure and facilities, especially the PARAM Brahma Supercomputer facility and the Microscopy facility. We acknowledge Vijay Vittal and Nisha Kurkure for their technical assistance. We thank Doiminique Bergmann, Adrienne Roeder, and Girish Deshpande for critically reading the manuscript and their inputs. We thank Ari Pekka Mähönen, Olivier Hamant, and Joris Sprakel for sharing the published materials. We thank Arun Sampathkumar for discussions. K.P. acknowledges Department of Biotechnology (DBT), Government of India (BT/PR41931/BRB/10/1964/2021), Science and Engineering Research Board-Scientific and Useful Profound Research Advancement (SERB-SUPRA), Government of India (SPR/2021/000109), and Indian Institute of Science Education and Research, Pune. K.T.T. and J.S. acknowledge VICI grant (VI.C.202.011 12268) by NWO. M.L.G.G. acknowledges the long-term program PlantXR: a new generation of breeding tools for extra-resilient crops (KICH3. LTP.20.005) by NWO and FFAR. R.S.S. was supported by a BBSRC Institute Strategic Programme grant (BB/X01102X/1) to the John Innes Centre. M.M.M. acknowledges PMRF and S.D. acknowledges CSIR for funding.

AUTHOR CONTRIBUTIONS

Conceptualization, M.M.M., K.T.T., and K.P.; data curation, M.M.M., J.S., S.D., K.R., B.L., R.S.S., B.C., M.L.G.G., K.T.T., and K.P.; formal analysis, M.M.M., J.S., S.D., K.R., B.L., R.S.S., V.W., M.L.G.G., B.C., B.S., K.T.T., and K.P.; funding acquisition, K.T.T. and K.P.; investigation: M.M.M., J.S., S.D., K.R., B.L., S.K., M.L.G.G., B.C., and K.T.T.; methodology, M.M.M., M.L.G.G., B.C., R.S.S., K.T.T., and K.P.; project administration, M.M.M., B.C., K.T.T., and K.P.; software, K.T.T., B.C., J.S., M.L.G.G., B.L., and R.S.S.; supervision, K.T.T., and K.P.; validation, M.M.M., S.D., and K.R.; visualization, M.M.M., J.S., S.D., K.R., B.C., M.L.G.G., and K.T.T.; writing – original draft, M.M.M., B.C., and K.T.T.; writing – review and editing, M.M.M., B.S., K.T.T., and K.P.

DECLARATION OF INTERESTS

The authors declare no competing interests.

STAR★METHODS

Detailed methods are provided in the online version of this paper and include the following:

- KEY RESOURCES TABLE
- EXPERIMENTAL MODEL AND STUDY PARTICIPANT DETAILS
  - Plant growth conditions
- METHOD DETAILS
  - Regeneration assay
  - Microscopic live imaging
  - Imaging after EdU staining
  - Treatments
  - EdU Staining using Click-It EdU imaging kit
  - Propidium Iodide staining
- QUANTIFICATION AND STATISTICAL ANALYSIS
  - Quantification of cell geometry distortion
  - Quantification of cell division frequency
  - Quantification of cell type and division frequency
  - Quantification of tapering root tip
  - Quantification of growth rates using ImageJ
  - Quantification of anisotropic growth
  - Statistical analysis

SUPPLEMENTAL INFORMATION

Supplemental information can be found online at https://doi.org/10.1016/j.cub.2025.06.072.

Received: March 11, 2025
Revised: June 2, 2025
Accepted: June 26, 2025
Published: July 24, 2025

REFERENCES

1. Coen, E., Rolland-Lagan, A.G., Matthews, M., Bangham, J.A., and Prusinkiewicz, P. (2004). The genetics of geometry. Proc. Natl. Acad. Sci. USA *101*, 4728–4735. https://doi.org/10.1073/pnas.0306308101.
2. Nelson, C.M. (2009). Geometric control of tissue morphogenesis. Biochim. Biophys. Acta *1793*, 903–910. https://doi.org/10.1016/J.BBAMCR.2008.12.014.
3. Coen, E., and Rebocho, A.B. (2016). Resolving Conflicts: Modeling Genetic Control of Plant Morphogenesis. Dev. Cell *38*, 579–583. https://doi.org/10.1016/J.DEVCEL.2016.09.006.
4. Cobham, A.E., and Mirth, C.K. (2020). The development of body and organ shape. BMC Zool. *5*, 1–15. https://doi.org/10.1186/S40850-020-00063-5.
5. Hamant, O., and Saunders, T.E. (2020). Shaping Organs: Shared Structural Principles across Kingdoms. Annu. Rev. Cell Dev. Biol. *36*, 385–410. https://doi.org/10.1146/annurev-cellbio-012820-103850.
6. Kelly-Bellow, R., Lee, K., Kennaway, R., Barclay, J.E., Whibley, A., Bushell, C., Spooner, J., Yu, M., Brett, P., Kular, B., et al. (2023). Brassinosteroid coordinates cell layer interactions in plants via cell wall and tissue mechanics. Science *380*, 1275–1281. https://doi.org/10.1126/science.adf0752.
7. Coen, E., and Cosgrove, D.J. (2023). The mechanics of plant morphogenesis. Science *379*, eade8055. https://doi.org/10.1126/science.ade8055.
8. Nath, U., Crawford, B.C.W., Carpenter, R., and Coen, E. (2003). Genetic control of surface curvature. Science *299*, 1404–1407. https://doi.org/10.1126/science.1079354.
9. Hernández-Hernández, V., Niklas, K.J., Newman, S.A., and Benítez, M. (2012). Dynamical patterning modules in plant development and evolution. Int. J. Dev. Biol. *56*, 661–674. https://doi.org/10.1387/IJDB.120027MB.
10. Whitewoods, C.D., and Coen, E. (2017). Growth and Development of Three-Dimensional Plant Form. Curr. Biol. *27*, R910–R918. https://doi.org/10.1016/j.cub.2017.05.079.
11. Hong, J.H., Savina, M., Du, J., Devendran, A., Kannivadi Ramakanth, K., Tian, X., Sim, W.S., Mironova, V.V., and Xu, J. (2017). A Sacrifice-for-Survival Mechanism Protects Root Stem Cell Niche from Chilling Stress. Cell *170*, 102–113.e14. https://doi.org/10.1016/J.CELL.2017.06.002.
12. Huang, C., Wang, Z., Quinn, D., Suresh, S., and Hsia, K.J. (2018). Differential growth and shape formation in plant organs. Proc. Natl. Acad. Sci. USA *115*, 12359–12364. https://doi.org/10.1073/pnas.1811296115.
13. Zhao, F., Du, F., Oliveri, H., Zhou, L., Ali, O., Chen, W., Feng, S., Wang, Q., Lü, S., Long, M., et al. (2020). Microtubule-Mediated Wall Anisotropy Contributes to Leaf Blade Flattening. Curr. Biol. *30*, 3972–3985.e6. https://doi.org/10.1016/J.CUB.2020.07.076.

14. Roeder, A.H.K. (2021). Arabidopsis sepals: A model system for the emergent process of morphogenesis. Quant. Plant Biol. *2*, e14. https://doi.org/10.1017/QPB.2021.12.

15. Trinh, D.C., Alonso-Serra, J., Asaoka, M., Colin, L., Cortes, M., Malivert, A., Takatani, S., Zhao, F., Traas, J., Trehin, C., et al. (2021). How Mechanical Forces Shape Plant Organs. Curr. Biol. *31*, R143–R159. https://doi.org/10.1016/J.CUB.2020.12.001.

16. Wilson-Sánchez, D., Bhatia, N., Runions, A., and Tsiantis, M. (2022). From genes to shape in leaf development and evolution. Curr. Biol. *32*, R1215–R1222. https://doi.org/10.1016/J.CUB.2022.09.021.

17. Varapparambath, V., Mathew, M.M., Shanmukhan, A.P., Radhakrishnan, D., Kareem, A., Verma, S., Ramalho, J.J., Manoj, B., Vellandath, A.R., Aiyaz, M., et al. (2022). Mechanical conflict caused by a cell-wall-loosening enzyme activates de novo shoot regeneration. Dev. Cell *57*, 2063–2080.e10. https://doi.org/10.1016/j.devcel.2022.07.017.

18. Cheng, J., Yao, X., Li, X., Yue, L., Duan, X., Li, B., Fu, X., Li, S., Shan, H., Yin, X., et al. (2023). Diversification of ranunculaceous petals in shape supports a generalized model for plant lateral organ morphogenesis and evolution. Sci. Adv. *9*, eadf8049. https://doi.org/10.1126/sciadv.adf8049.

19. Satterlee, J.W., Evans, L.J., Conlon, B.R., Conklin, P., Martinez-Gomez, J., Yen, J.R., Wu, H., Sylvester, A.W., Specht, C.D., Cheng, J., et al. (2023). A Wox3-patterning module organizes planar growth in grass leaves and ligules. Nat. Plants *9*, 720–732. https://doi.org/10.1038/S41477-023-01405-0.

20. Keller, R. (2002). Shaping the vertebrate body plan by polarized embryonic cell movements. Science *298*, 1950–1954. https://doi.org/10.1126/science.1079478.

21. Solnica-Krezel, L. (2005). Conserved Patterns of Cell Movements during Vertebrate Gastrulation. Curr. Biol. *15*, R213–R228. https://doi.org/10.1016/J.CUB.2005.03.016.

22. Hong, L., Dumond, M., Tsugawa, S., Sapala, A., Routier-Kierzkowska, A. L., Zhou, Y., Chen, C., Kiss, A., Zhu, M., Hamant, O., et al. (2016). Variable Cell Growth Yields Reproducible Organ Development through Spatiotemporal Averaging. Dev. Cell *38*, 15–32. https://doi.org/10.1016/J.DEVCEL.2016.06.016.

23. Adorada, D.L., Biles, C.L., Liddell, C.M., Fernández-Pavía, S., Waugh, K. O., and Waugh, M.E. (2000). Disease development and enhanced susceptibility of wounded pepper roots to phytophthora capsici. Plant Pathol. *49*, 719–726. https://doi.org/10.1046/j.1365-3059.2000.00510.x.

24. Colombi, T., Kirchgessner, N., Walter, A., and Keller, T. (2017). Root Tip Shape Governs Root Elongation Rate under Increased Soil Strength. Plant Physiol. *174*, 2289–2301. https://doi.org/10.1104/PP.17.00357.

25. Potocka, I., and Szymanowska-Pulka, J. (2018). Morphological responses of plant roots to mechanical stress. Ann. Bot. *122*, 711–723. https://doi.org/10.1093/AOB/MCY010.

26. Marconi, M., Gallemi, M., Benkova, E., and Wabnik, K. (2021). A coupled mechano-biochemical model for cell polarity guided anisotropic root growth. eLife *10*, e72132. https://doi.org/10.7554/eLife.72132.

27. Grieneisen, V.A., Xu, J., Marée, A.F.M., Hogeweg, P., and Scheres, B. (2007). Auxin transport is sufficient to generate a maximum and gradient guiding root growth. Nature *449*, 1008–1013. https://doi.org/10.1038/nature06215.

28. Mironova, V.V., Omelyanchuk, N.A., Yosiphon, G., Fadeev, S.I., Kolchanov, N.A., Mjolsness, E., and Likhoshvai, V.A. (2010). A plausible mechanism for auxin patterning along the developing root. BMC Syst. Biol. *4*, 98. https://doi.org/10.1186/1752-0509-4-98.

29. Band, L.R., Wells, D.M., Fozard, J.A., Ghetiu, T., French, A.P., Pound, M. P., Wilson, M.H., Yu, L., Li, W., Hijazi, H.I., et al. (2014). Systems Analysis of Auxin Transport in the Arabidopsis Root Apex. Plant Cell *26*, 862–875. https://doi.org/10.1105/TPC.113.119495.

30. De Vos, D., Vissenberg, K., Broeckhove, J., and Beemster, G.T.S. (2014). Putting Theory to the Test: Which Regulatory Mechanisms Can Drive Realistic Growth of a Root? PLoS Comput. Biol. *10*, e1003910. https://doi.org/10.1371/JOURNAL.PCBI.1003910.

31. Mähönen, A.P., Ten Ten Tusscher, K., Siligato, R., Smetana, O., Díaz-Triviño, S., Salojärvi, J., Wachsman, G., Prasad, K., Heidstra, R., and Scheres, B. (2014). PLETHORA gradient formation mechanism separates auxin responses. Nature *515*, 125–129. https://doi.org/10.1038/nature13663.

32. Jensen, O.E., and Fozard, J.A. (2015). Multiscale Models in the Biomechanics of Plant Growth. Physiology *30*, 159–166. https://doi.org/10.1152/PHYSIOL.00030.2014.

33. Morales-Tapia, A., and Ruz-Ramírez, A. (2016). Computational modeling of auxin: A foundation for plant engineering. Front. Plant Sci. *7*, 1881. https://doi.org/10.3389/fpls.2016.01881.

34. Rutten, J.P., and ten Tusscher, K. (2019). In Silico Roots: Room for Growth. Trends Plant Sci. *24*, 250–262. https://doi.org/10.1016/j.tplants.2018.11.005.

35. Salvi, E., Rutten, J.P., Di Mambro, R., Polverari, L., Licursi, V., Negri, R., Dello Ioio, R., Sabatini, S., and Ten Tusscher, K. (2020). A Self-Organized PLT/Auxin/ARR-B Network Controls the Dynamics of Root Zonation Development in Arabidopsis thaliana. Dev. Cell *53*, 431–443.e23. https://doi.org/10.1016/j.devcel.2020.04.004.

36. Fridman, Y., Strauss, S., Horev, G., Ackerman-Lavert, M., Reiner-Benaim, A., Lane, B., Smith, R.S., and Savaldi-Goldstein, S. (2021). The root meristem is shaped by brassinosteroid control of cell geometry. Nat. Plants *7*, 1475–1484. https://doi.org/10.1038/s41477-021-01014-9.

37. Xu, J., Hofhuis, H., Heidstra, R., Sauer, M., Friml, J., and Scheres, B. (2006). A molecular framework for plant regeneration. Science *311*, 385–388. https://doi.org/10.1126/SCIENCE.1121790.

38. Birnbaum, K.D., and Sánchez Alvarado, A.S. (2008). Slicing across Kingdoms: Regeneration in Plants and Animals. Cell *132*, 697–710. https://doi.org/10.1016/J.CELL.2008.01.040.

39. Efroni, I., Mello, A., Nawy, T., Ip, P.L., Rahni, R., Delrose, N., Powers, A., Satija, R., and Birnbaum, K.D. (2016). Root Regeneration Triggers an Embryo-like Sequence Guided by Hormonal Interactions. Cell *165*, 1721–1733. https://doi.org/10.1016/j.cell.2016.04.046.

40. Durgaprasad, K., Roy, M.V., Venugopal M, A., Kareem, A., Raj, K., Willemsen, V., Mähönen, A.P., Scheres, B., and Prasad, K. (2019). Gradient Expression of Transcription Factor Imposes a Boundary on Organ Regeneration Potential in Plants. Cell Rep. *29*, 453–463.e3. https://doi.org/10.1016/j.celrep.2019.08.099.

41. Sena, G., Wang, X., Liu, H.Y., Hofhuis, H., and Birnbaum, K.D. (2009). Organ regeneration does not require a functional stem cell niche in plants. Nature *457*, 1150–1153. https://doi.org/10.1038/NATURE07597.

42. Canher, B., Heyman, J., Savina, M., Devendran, A., Eekhout, T., Vercauteren, I., Prinsen, E., Matosevich, R., Xu, J., Mironova, V., et al. (2020). Rocks in the auxin stream: Wound-induced auxin accumulation and ERF115 expression synergistically drive stem cell regeneration. Proc. Natl. Acad. Sci. USA *117*, 16667–16677. https://doi.org/10.1073/pnas.2006620117.

43. Mathew, M.M., and Prasad, K. (2021). Model systems for regeneration: Arabidopsis. Development *148*, dev195347. https://doi.org/10.1242/dev.195347.

44. Razzell, W., Wood, W., and Martin, P. (2014). Recapitulation of morphogenetic cell shape changes enables wound re-epithelialisation. Development *141*, 1814–1820. https://doi.org/10.1242/DEV.107045/-/DC1.

45. Tetley, R.J., Staddon, M.F., Heller, D., Hoppe, A., Banerjee, S., and Mao, Y. (2019). Tissue fluidity promotes epithelial wound healing. Nat. Phys. *15*, 1195–1203. https://doi.org/10.1038/s41567-019-0618-1.

46. Ton, A.T., MacKeith, A.K., Shattuck, M.D., and O'Hern, C.S. (2024). Mechanical plasticity of cell membranes enhances epithelial wound closure. Phys. Rev. Research *6*, L012036. https://doi.org/10.1103/PhysRevResearch.6.L012036.

47. Mishra, A.K., Tramacere, F., Guarino, R., Pugno, N.M., and Mazzolai, B. (2018). A study on plant root apex morphology as a model for soft robots moving in soil. PLoS One *13*, e0197411. https://doi.org/10.1371/journal.pone.0197411.

48. Lee, L.R., Guillotin, B., Rahni, R., Hutchison, C., Desvoyes, B., Gutierrez, C., and Birnbaum, K.D. (2024). Glutathione accelerates the cell cycle and cellular reprogramming in plant regeneration. Preprint at bioRxiv, 2023.11.28.569014. https://doi.org/10.1101/2023.11.28.569014.

49. Simon, M.L.A., Platre, M.P., Marquès-Bueno, M.M., Armengot, L., Stanislas, T., Bayle, V., Caillaud, M.C., and Jaillais, Y. (2016). A PtdIns(4)P-driven electrostatic field controls cell membrane identity and signalling in plants. Nat. Plants *2*, 16089. https://doi.org/10.1038/NPLANTS.2016.89.

50. Wolf, S., Mravec, J., Greiner, S., Mouille, G., and Höfte, H. (2012). Plant cell wall homeostasis is mediated by brassinosteroid feedback signaling. Curr. Biol. *22*, 1732–1737. https://doi.org/10.1016/j.cub.2012.07.036.

51. Müller, K., Levesque-Tremblay, G., Bartels, S., Weitbrecht, K., Wormit, A., Usadel, B., Haughn, G., and Kermode, A.R. (2013). Demethylesterification of Cell Wall Pectins in Arabidopsis Plays a Role in Seed Germination. Plant Physiol. *161*, 305–316. https://doi.org/10.1104/PP.112.205724.

52. Di Fino, L.M., Anjam, M.S., Besten, M., Mentzelopoulou, A., Papadakis, V., Zahid, N., Baez, L.A., Trozzi, N., Majda, M., Ma, X., et al. (2025). Cellular damage triggers mechano-chemical control of cell wall dynamics and patterned cell divisions in plant healing. Dev. Cell *60*, 1411–1422.e6. https://doi.org/10.1016/j.devcel.2024.12.032.

53. Stöckle, D., Reyes-Hernández, B.J., Barro, A.V., Nenadić, M., Winter, Z., Marc-Martin, S., Bald, L., Ursache, R., Fujita, S., Maizel, A., et al. (2022). Microtubule-based perception of mechanical conflicts controls plant organ morphogenesis. Sci. Adv. *8*, eabm4974. https://doi.org/10.1126/sciadv.abm4974.

54. Scheres, B., Di Laurenzio, L.D., Willemsen, V., Hauser, M.-T., Janmaat, K., Weisbeek, P., and Benfey, P.N. (1995). Mutations affecting the radial organisation of the Arabidopsis root display specific defects throughout the embryonic axis. Development *121*, 53–62. https://doi.org/10.1242/dev.121.1.53.

55. Mähönen, A.P., Bonke, M., Kauppinen, L., Riikonen, M., Benfey, P.N., and Helariutta, Y. (2000). A novel two-component hybrid molecule regulates vascular morphogenesis of the Arabidopsis root. Genes Dev. *14*, 2938–2943. https://doi.org/10.1101/GAD.189200.

56. Ohashi-Ito, K., and Bergmann, D.C. (2007). Regulation of the Arabidopsis root vascular initial population by LONESOME HIGHWAY. Development *134*, 2959–2968. https://doi.org/10.1242/DEV.006296.

57. Chan, J., and Coen, E. (2020). Interaction between Autonomous and Microtubule Guidance Systems Controls Cellulose Synthase Trajectories. Curr. Biol. *30*, 941–947.e2. https://doi.org/10.1016/j.cub.2019.12.066.

58. Collings, D.A., Lill, A.W., Himmelspach, R., and Wasteneys, G.O. (2006). Hypersensitivity to cytoskeletal antagonists demonstrates microtubule–microfilament cross-talk in the control of root elongation in Arabidopsis thaliana. New Phytol. *170*, 275–290. https://doi.org/10.1111/j.1469-8137.2006.01671.x.

59. Chakrabortty, B., Blilou, I., Scheres, B., and Mulder, B.M. (2018). A computational framework for cortical microtubule dynamics in realistically shaped plant cells. PLoS Comput. Biol. *14*, e1005959. https://doi.org/10.1371/journal.pcbi.1005959.

60. Chakrabortty, B., Willemsen, V., de Zeeuw, T., Liao, C.-Y., Weijers, D., Mulder, B., and Scheres, B. (2018). A Plausible Microtubule-Based Mechanism for Cell Division Orientation in Plant Embryogenesis. Curr. Biol. *28*, 3031–3043.e2. https://doi.org/10.1016/j.cub.2018.07.025.

61. Louveaux, M., Julien, J.D., Mirabet, V., Boudaoud, A., and Hamant, O. (2016). Cell division plane orientation based on tensile stress in Arabidopsis thaliana. Proc. Natl. Acad. Sci. USA *113*, E4294–E4303. https://doi.org/10.1073/pnas.1600677113.

62. Rahni, R., Guillotin, B., Lee, L.R., and Birnbaum, K.D. (2024). A temporal map of division, chromatin modification, and identity specification in the regenerating Arabidopsis root. Preprint at bioRxiv. https://doi.org/10.1101/2024.01.09.574680.

63. Blilou, I., Xu, J., Wildwater, M., Willemsen, V., Paponov, I., Friml, J., Heidstra, R., Aida, M., Palme, K., and Scheres, B. (2005). The PIN auxin efflux facilitator network controls growth and patterning in Arabidopsis roots. Nature *433*, 39–44. https://doi.org/10.1038/nature03184.

64. Matosevich, R., Cohen, I., Gil-Yarom, N., Modrego, A., Friedlander-Shani, L., Verna, C., Scarpella, E., and Efroni, I. (2020). Local auxin biosynthesis is required for root regeneration after wounding. Nat. Plants *6*, 1020–1030. https://doi.org/10.1038/s41477-020-0737-9.

65. Hamant, O., Heisler, M.G., Jönsson, H., Krupinski, P., Uyttewaal, M., Bokov, P., Corson, F., Sahlin, P., Boudaoud, A., Meyerowitz, E.M., et al. (2008). Developmental patterning by mechanical signals in Arabidopsis. Science *322*, 1650–1655. https://doi.org/10.1126/SCIENCE.1165594.

66. Schindelin, J., Arganda-Carreras, I., Frise, E., Kaynig, V., Longair, M., Pietzsch, T., Preibisch, S., Rueden, C., Saalfeld, S., Schmid, B., et al. (2012). Fiji: An open-source platform for biological-image analysis. Nat. Methods *9*, 676–682. https://doi.org/10.1038/nmeth.2019.

67. Thévenaz, P., Ruttimann, U.E., and Unser, M. (1998). A pyramid approach to subpixel registration based on intensity. IEEE Trans. Image Process. *7*, 27–41. https://doi.org/10.1109/83.650848.

68. de Reuille, P.B., Routier-Kierzkowska, A.L., Kierzkowski, D., Bassel, G.W., Schüpbach, T., Tauriello, G., Bajpai, N., Strauss, S., Weber, A., Kiss, A., et al. (2015). MorphoGraphX: A platform for quantifying morphogenesis in 4D. eLife *4*, 05864. https://doi.org/10.7554/eLife.05864.

69. Kareem, A., Durgaprasad, K., Sugimoto, K., Du, Y., Pulianmackal, A.J., Trivedi, Z.B., Abhayadev, P.V., Pinon, V., Meyerowitz, E.M., Scheres, B., et al. (2015). PLETHORA Genes Control Regeneration by a Two-Step Mechanism. Curr. Biol. *25*, 1017–1030. https://doi.org/10.1016/J.CUB.2015.02.022.

70. Wolny, A., Cerrone, L., Vijayan, A., Tofanelli, R., Barro, A.V., Louveaux, M., Wenzl, C., Strauss, S., Wilson-Sánchez, D., Lymbouridou, R., et al. (2020). Accurate and versatile 3D segmentation of plant tissues at cellular resolution. eLife *9*, e57613. https://doi.org/10.7554/eLife.57613.

71. Hernandez-Lagana, E., Mosca, G., Mendocilla-Sato, E., Pires, N., Frey, A., Giraldo-Fonseca, A., Michaud, C., Grossniklaus, U., Hamant, O., Godin, C., et al. (2021). Organ geometry channels reproductive cell fate in the Arabidopsis ovule primordium. eLife *10*, e66031. https://doi.org/10.7554/eLife.66031.

72. Ávalos-Rangel, A., Ruiz-Herrera, L.F., Gutiérrez-Alanis, D., Herrera-Estrella, L., Raya-González, J., and López-Bucio, J. (2024). CLE14 Peptide Impairs Root Tip Regeneration and Callogenesis in Arabidopsis. J. Plant Growth Regul. *43*, 1458–1465. https://doi.org/10.1007/s00344-023-11197-4.

73. Dixit, R., and Cyr, R. (2004). Encounters between Dynamic Cortical Microtubules Promote Ordering of the Cortical Array through Angle-Dependent Modifications of Microtubule Behavior. Plant Cell *16*, 3274–3284. https://doi.org/10.1105/TPC.104.026930.

74. Ambrose, C., Allard, J.F., Cytrynbaum, E.N., and Wasteneys, G.O. (2011). A CLASP-modulated cell edge barrier mechanism drives cell-wide cortical microtubule organization in Arabidopsis. Nat. Commun. *2*, 430. https://doi.org/10.1038/ncomms1444.

75. Hawkins, T., Mirigian, M., Selcuk Yasar, M., and Ross, J.L. (2010). Mechanics of microtubules. J. Biomech. *43*, 23–30. https://doi.org/10.1016/J.JBIOMECH.2009.09.005.

76. Deinum, E.E., Tindemans, S.H., and Mulder, B.M. (2011). Taking directions: the role of microtubule-bound nucleation in the self-organization of the plant cortical array. Phys. Biol. *8*, 056002. https://doi.org/10.1088/1478-3975/8/5/056002.

77. Boudaoud, A., Burian, A., Borowska-Wykręt, D., Uyttewaal, M., Wrzalik, R., Kwiatkowska, D., and Hamant, O. (2014). FibrilTool, an ImageJ plug-in to quantify fibrillar structures in raw microscopy images. Nat. Protoc. *9*, 457–463. https://doi.org/10.1038/nprot.2014.024.

STAR★METHODS

KEY RESOURCES TABLE

REAGENT or RESOURCE	SOURCE	IDENTIFIER
Chemicals, peptides, and recombinant proteins		
Murashige & Skoog basal salts Medium	Sigma	Cat# M5524
Plant-agar	HiMedia	Cat# PCT0901
Sucrose	Sigma	Cat# S0389
Dimethyl-sulfoxide	Sigma	Cat# D8418
Propidium iodide	Sigma	Cat# P4170
Ampicillin	Sigma	Cat# A0166
2,3-BUTANEDIONE MONOXIME >= 98%	Sigma	Cat# B0753-25G
Oryzalin PESTANAL	Sigma	Cat# 36182
16% Formaldehyde Methanol free	Thermo	Cat# 28908
Triton X-100	Sigma	Cat# X100-500ml
Calcofluor White (Fluorescent Brightener 28)	Sigma	Cat# F3543-1G
Click-It EdU Alexa Fluor 647 imaging kit	Invitrogen	Cat# C10340
BSA	HiMedia	Cat# TC545-100G
Deposited data		
MorphoMechanX model for 2D simulations of a growing root tip during regeneration	Current Study	Zenodo: https://doi.org/10.5281/zenodo.15698229
Raw and analyzed data	Current Study	https://doi.org/10.17632/vyyvby3hv2.1
Experimental models: Organisms/strains		
Arabidopsis thaliana: Col-0	Nottingham Arabidopsis Stock Centre	N/A
A.thaliana: Columbia; *pUBQ::mCIT-KA1*^{MARK1}	Simon et al.[49]	NASC#2107345
A. thaliana: Columbia; *woodenleg*	ABRC	CS9817
A. thaliana: Columbia *pWOX5::gWOX5:erGFP*	Xu et al.[37]	N/A
A. thaliana: Columbia; *35S::PMEi5*	Müller et al.[51]	N/A
A. thaliana: Columbia; *pG1090:XVE::axr3-1-RFP*	Mähönen et al.[31]	N/A
A. thaliana: Columbia; *35S::GFP-MBD*	Hamant et al.[65]	N/A
Software and algorithms		
FIJI	Schindelin, J. et al.[66]	https://imagej.net/software/fiji; RRID: SCR_003070
Stackreg	Thévenaz et al.[67]	N/A
MorphoGraphX 2.0	de Reuille et al.[68]	N/A
GraphPad Prism10	https://www.graphpad.com	N/A
Huygens Professional	https://svi.nl⟩ Huygens-Professional	N/A
Adobe Photoshop 2025	Adobe Acrobat	N/A
Adobe Illustrator	Adobe Acrobat	N/A
Other		
Growth chamber	Percivial	N/A
Leica TCS SP8 with Multiphoton	Leica	N/A
Olympus FV4000	Olympus	N/A
Zeiss LSM 780	Zeiss	N/A
Zeiss Axio Scope.A1	Zeiss	N/A

EXPERIMENTAL MODEL AND STUDY PARTICIPANT DETAILS

The Columbia ecotype of *Arabidopsis thaliana*[69] was used as a wildtype for this study. The *Arabidopsis* mutant *wol* has been previously described.[54,55]

Plant growth conditions

Surface sterilization of the *Arabidopsis thaliana* seeds was done using 70% ethanol followed by 20% sodium hypochlorite. The seeds were then washed with distilled autoclaved water seven times and stored at 4°C for 4 days for the vernalization process. The seeds were plated on half-strength Murashige and Skoog (MS) growth medium with 0.8% plant-based agar and grown under 45 μmol/m2/s long day (16Hrs light/8Hrs dark) condition at 22°C and 70% relative humidity.

METHOD DETAILS

Regeneration assay

Root tip resection and the regeneration assay were performed as previously described.[40] The root tip regeneration assay was done on 4-day-old seedlings. The seedlings were carefully placed on a sterile glass slide with a few drops of sterile water. Their root tips were manually resected using the sharp tip of a sterile 1ml syringe (Dispovan) under a Zeiss Axio Scope.A1 microscope. The resection was performed within the root meristem, from the QC till the elongation zone. In wild type, high and low cuts were defined by the distance from the fourth tier of the columella cells to the cut site. Low cuts were between 120 and 210μm, whereas high cuts were between 250 and 300μm. Meanwhile, resections in mutants with shorter meristems were made within in the meristematic zone with dividing cells. Post resection, an image of the detached root tip section was captured immediately to determine the position of the cut. Following that, the resected seedlings were either returned to MS medium or prepared for confocal imaging. The root tip regeneration was evaluated based on the growth and morphology of the root tip at 5-days post-cut.

Microscopic live imaging

Live imaging of the regenerating root was done using the Leica TCS SP8 Multiphoton, Zeiss LSM 780, and Olympus FV4000 laser scanning microscope. The resected seedlings were mounted on a sterile glass slide with a few drops of filter-sterilized 20μg/ml propidium iodide (PI). Time-lapse images of the middle plane of the root tip were acquired using a 20X air objective lens. Post imaging, the seedlings were placed back on MS media in the same orientation as when they were mounted. The resected seedlings were followed for 5 days. Time-lapse imaging for MGX segmentation and analysis was done using a 63X oil immersion objective lens. The middle plane of the root was captured with z-stacks of at least 15 slices, thus covering the entire cell file at that plane. For imaging using 20X objective, 10-30% laser power was used (488nm- for GFP and mCIT, 561nm- for PI as excitation wavelength). Master gain was set between 10-100 for HyD detectors and 600-800 for PMT-based detectors. The pinhole was set at 1AU, with a frame size of 1024 by 512 pixels, line-averaging set to 2-3, and zoom factor set at a range of 1.2 to 1.5. For imaging using the 63X objective, 20-30% laser power was used, and master gain was set between 90-150 for HyD-based detectors and 600-800 for PMT-based detectors. The pinhole was set at 1-1.2AU, along with a frame size of 1024 by 1024 pixels, line averaging set to 2 and the zoom factor set at a range of 0.75-1.2. For imaging single cells for principal growth direction analysis, the zoom factor was changed to 6-9 based on the ROI of the cell. All z-stacks were taken with a step size ranging from 0.3μm-0.6μm based on the cell size.

For cytoskeleton imaging, the *35S:GFP-MBD* in WT line was used. The resected roots of this line were imaged using Leica TCS SP8 multiphoton microscope at various time points. The resected roots were stained using PI and mounted with few drops of water on a clear glass slide. For imaging *35S:GFP-MBD* a tuneable multiphoton laser was set at 960nm wavelength. Imaging was done using a 20x objective, with the 960nm laser set at 20-40% power, depending on the thickness of the sample. The signal was collected using a HyD detector with gain set between 400-500. The pinhole for the multiphoton imaging was set at full limit. For the imaging PI-stained cell wall, the microscopic parameters were set as described previously. The GFP and PI channels were imaged sequentially. The frame size was set at 1024 by 1024 pixels, with a line averaging of 4 and bidirectional scan speed set at 200 Hz.

Imaging after EdU staining

Prepared samples were mounted on few drops of 1X PBS for imaging under the Olympus FV4000 confocal microscope. The 640nm laser was used to excite the EdU-AlexaFluor647 and 405nm laser was used to excite Calcofluor white. Imaging was performed at a laser power of 10-20% for the 640nm laser and at 0.2-0.5% for the 405nm laser. The frame size was set at 1024 by 768 pixels, with line averaging of 3 and scan speed set at 4μs per pixel.

Treatments

Laser targeted cell ablation

The samples were prepared as similar to live imaging. Fully resolved cells were chosen for ablation using the FRAP module of the Leica TCS SP8 multiphoton microscope at wavelength 900nm and 80% laser power. Once the cell of interest is in focus in 63X oil magnification, an ROI was drawn in the middle of the cell using the ROI tool. Ablation was performed with the setting for bleaching, where the iterations for the pre-bleach, bleach, and post bleach were 1, 50, and 2 respectively. The line average was kept at 1. If the cell is not ablated, the cycle was repeated after 30 seconds.

Estradiol treatment

In case of *pG1090i::axr3-1-RFP* in WT, 3dpg old seedlings were transferred to half strength MS medium supplemented with 5μM estradiol and were incubated for 24 hours, before resection. Post resection, the cut roots were placed on estradiol free half strength MS medium. In case of control, the 3dpg seedlings were transferred to half strength MS medium supplemented with DMSO for 24 hours, before resection.

BDM treatment

2,3-BUTANEDIONE MONOXIME (BDM) was dissolved in sterile water and filter sterilized to make a 0.5M stock solution. This was added to autoclaved half-strength MS media to a final concentration of 7mM. Post resection, the seedlings were placed in the MS media plates containing 7mM BDM for 5 days till scoring of the roots for regeneration. For time-lapse live imaging of BDM-treated roots, 7mM BDM +PI (20μg/ml) solution was made to stain the sample, and 7mM BDM solution in sterile water was used to wash the sample post-imaging.

Oryzalin treatment

The stock solution of Oryzalin was made in DMSO at a concentration of 30mM and filter sterilized. It was added to autoclaved half-strength MS media at a concentration of 30μM. Post resection, the seedlings were placed in the oryzalin-containing MS media for 24 hours for treatment. After 24 hours of treatment, the seedlings were removed from the Oryzalin-containing media, washed thoroughly with sterile water 3-4 times, and then placed in a fresh half-strength MS media plate for 4 days till scoring of the roots for regeneration.

EdU Staining using Click-It EdU imaging kit

Resected roots of 4dpg WT and *wol* mutant seedlings were incubated for 2 hours in liquid ½-MS media in growth chamber. For incubation, 2ml of liquid ½-MS in each well of a 6 well culture plate containing 20 seedlings was used. After 2 h, the liquid ½-MS in each well was replaced with 1ml liquid ½-MS containing 5μM EdU. The seedlings were incubated in the media containing EdU for 10hrs in the growth chamber (chase period). After the chase period the seedlings were thoroughly washed with fresh liquid ½-MS twice. The samples were then fixed using 3.7% Formaldehyde and 1% Triton X-100 in 1X PBS solution. For fixation, 500ul of fixative solution was used per well of a 12 well cell culture plate containing 20 seedlings. The samples were incubated in the fixative solution for 1 h in a nutating shaker. After fixation, the seedlings were washed twice using 3%BSA in 1X PBS solution for 10 minutes each on the shaker. The samples were then washed once with 1X PBST (0.3% Triton) for 10 min on the shaker. During the last wash, the Click Reaction mixture was prepared as per protocol provided with the Kit (Invitrogen: C10340). 150μl of the Click reaction mixture was used per well containing the samples. The samples were then incubated for 1 h in dark on the shaker. All further steps were carried out in dark condition after this point. The samples were washed thrice with 1X PBST for 15 minutes each. For co-staining the samples, 1X PBST containing 0.1% Calcofluor white was prepared. The samples were then incubated for 10 min with 150ul of the freshly prepared staining solution per well. After staining with Calcofluor white, the samples were washed twice with 1X PBST for 10 min each. Finally, the samples were stored in 1X PBS at 4° till imaging. For imaging samples were mounted on clear glass slide on few drops on 1X PBS as mounting medium and then imaged under a confocal microscope.

Propidium Iodide staining

The stock solution of PI was made by dissolving it in sterile distilled water at a concentration of 2.5mg/ml. The seedlings were treated with 20μg/ml filter-sterilized PI solution for 2 minutes on a sterile glass slide to stain the cell wall. After staining, the root was mounted with a few more drops of PI so the coverslip would not trap any air bubbles. Excess PI was drained from the side using a tissue paper and the root was imaged under the confocal laser scanning microscope. Post imaging, the coverslip was gently removed and the root was washed thoroughly with sterile water 3-4 times by dripping drops of water down the slide to remove the stain before further incubation in the growth chamber to capture live images at different time points.

QUANTIFICATION AND STATISTICAL ANALYSIS

Quantification of cell geometry distortion

To determine the extent of distortion in cell shape, we chose to measure three aspects of cell geometry, including i) the exterior deformation angles, ii) the two adjacent interior angles of a cell and iii) its aspect ratio. The roots were stained with propidium iodide to visualize the cell boundaries. The angles were quantified using the angle tool in Fiji/ImageJ. Prior to quantification, it was ensured that the root's longitudinal axis was oriented exactly parallel to the Y axis of the image frame. The orientation of the longitudinal axis with respect to the frame was checked using the angle tool. If any deviation was found, it was corrected using the "rotate" tool in ImageJ before further analysis. The mid-plane of a cell was chosen for all the quantifications. The angle tool was used to quantify (i) and (ii).

For measuring the exterior deformation angles, we considered the two cell edges that lie parallel to the root diameter under developmental conditions. The angles γ, ε, γ'and ε' were measured with respect to the horizontal axis of the root. The exact positions where these angles were measured can be seen in Figure 1O. The cell's internal angles (α and α') were measured at two adjacent vertices opposite to the cut end. For aspect ratio measurement, we selected "shape descriptor" under the "Set measurements" option in the Analyze tab. Further, we marked each cell using the "polygon selections" tool to obtain the cell's aspect ratio (AR). All three parameters were measured around 19 hours post-cut, when these deformations were prominent and were quantified for cells in all four zones (A^{cut}/RCZ, B^{cut}, A^{uncut}, and B^{uncut}).

Quantification of cell division frequency

Newly dividing cells in regenerating roots were visualised using *pUBQ::mCIT- KA1*^{MARK1} in WT which marks the newly forming cell plate. Time-lapse imaging of regenerating *pUBQ::mCIT-KA1*^{MARK1} roots stained with PI was acquired in Zeiss LSM 780 and Leica TCS SP8 confocal laser-scanning microscopes. Cell division was categorized into periclinal, anticlinal, oblique, and diagonal divisions. The number of cell divisions for each category was quantified using z-stack images covering the middle plane of the root. The time window for this quantification was restricted from 10 -20 hpc when diagonal divisions are predominant.

Quantification of cell type and division frequency

PI-stained roots of wildtype, mutants, and roots treated with pharmacological drugs were imaged for quantification. The number of rhomboidal cells and the cells undergoing diagonal division were counted across a time frame of 10-20 hpc. In case of visual ambiguity in selecting rhomboidal cells, the exterior and internal angles of the cells were measured and used as a basis for selection. In a rhomboidal cell, the internal angles are expected to be obtuse on the side nearest to the stele and acute at the adjacent vertex.

Quantification of tapering root tip

To measure the initiation of root tapering, two distinct approaches were used (Figures 6U–6X). Both relative change in diameter across root length and angle of tapering were performed using Fiji/ImageJ. The z-stack images covering the middle plane of the PI-stained roots were used to quantify both root and stele diameters. The diameter of the root was measured edge-edge between two opposite epidermal cells at two different positions in the root, thus yielding two values D and D′. The diameter of the root near the cut end is denoted by D. When measuring "D" the first cell close to the cut end was used as a reference point. Meanwhile, D′ is measured at the base of the elongation zone. D'/D represents the ratio of the root's diameter between the cut end and the transition zone. The same method was used to determine the diameters A and A' across the stele. However, in this case, the diameter was measured between the two pericycle cell files. Furthermore, because the stelar cells immediately adjacent to the cut end were difficult to visualize, "A" was quantified using the first pericycle cell layer, whose cell borders were clearly visible. In addition, the angle of root tapering (θ) was determined using the angle tool in ImageJ to quantify the regenerating root's divergence from the vertical axis. We chose the 0 – 20 hpc time window to compare the changes in D'/D and A'/A in order to clearly capture the initiation of tapering of regenerating roots.

Quantification of growth rates using ImageJ

Growth rate of individual cells

Growth rate measurements were done by taking into account both cell expansion and cytoplasmic growth of dividing cells. The difference in a cell's diagonal length measured at two different times was used to calculate the cell's growth rate. Using the line tool in ImageJ, we chose to measure the diagonal that faced toward the centre of the root. In order to rule out the effect of cell size, the growth rate was normalized to the initial length of its diagonal. Thus, the normalized growth rate was calculated as $((L_f - L_i) / L_i) *100$, where Li was the length of the diagonal at the initial time point and L_f was the length of the diagonal at the last time point selected. Cells belonging to three distinct cell files namely, epidermis/outer cell layer, cortex/middle cell layer and endodermis/inner cell layer, were used for this quantification. Growth rate for wildtype cut roots was calculated twice. The first measurement was done during the first phase of root tip restoration by taking 10-18 hpc as our time frame. We then measured the growth rate of regenerating wildtype roots, between 48 - 56 hpc. In addition, the growth rate calculation of resected *wol* mutant roots and uncut wildtype roots were also performed between 10-18 hpc. The cells located within 70 μm of the cut end of the root were measured for all quantifications. The cells for uncut roots were chosen from ≈150μm above the fourth tier of columella and within 70 μm from this region. As with earlier quantifications, only cells in the middle plane of the root were considered.

Growth rate of cell files after segmentation

PlantSeg was used to process the z-stack images with a convolutional neural network for cell wall stain-based cell boundary prediction as described in Wolny et al.[70]. The resulting images were then used in Fiji to measure the length spanning from one cell to another within a tissue layer of uncut and cut roots at different timepoints. To calculate the percentage of growth we divided the difference between the final and the starting lengths by the starting value.

Principal Growth Direction Analysis

To perform the principal growth direction analysis of a cortical cell at 9 and 19 hpc we used MorphoGraphX (as described in de Reuille et al.[68]). First, we created a surface mesh using a marching cubes algorithm, in which the fluorescence signal was projected for the manual segmentation of individual cells using the watershed segmentation method. The resulting segmented surface meshes were then used to identify the corresponding cortical and neighbours' cells in the 9 and 19 hpc images. Next, we used the principal direction of growth method from MGX, and displayed the scaled StretchMax and StrecthMin showing the deformation in the maximal and the minimal direction, respectively.

Quantification of anisotropic growth

Manual quantification

The direction of cell growth was assessed on the middle plane of cells exhibiting geometric deformation. The cell boundaries were outlined using the polygon tool in ImageJ. Following this, the line tool was used to measure the edge-to-edge length of the cell's diagonals. The aspect ratio for each cell was calculated by dividing the length of the major diagonal axis (pointing towards the root

center) by the minor axis. The aspect ratio was determined at two time points, between 10- and 18-hours post-cut, with a 5-6 hour interval between the two measurements. The difference in aspect ratio over time was estimated to assess whether cell growth was anisotropic.

Model structure for simulating growth rate differences

The model was implemented in the MorphoMechanX framework[71] It consists of two-dimensional structures at two distinct scales. At a larger scale is the division of the root into cells; in turn, each cell is refined into triangular finite elements of approximately equal size (here about 2 μm). Individual cells have a cell type and are initially arranged in files (Figure 4A). The finite elements, taken together, form a mesh covering the organ and are used in a finite element method (FEM) simulation to determine how growth will reshape the geometry of the root.

During a simulation, each cell is assigned a target growth depending on its cell type. It expresses this growth by increasing the size of the rest configuration of each of its refining elements at each growth step. The FEM simulation is run to resolve the possibly incompatible target growths into a resultant growth for each element. A linear isotropic St. Venant material model was used, parameterized by a Young's modulus of 100 MPa and a Poisson ratio of 0.3. After each growth step is resolved to a mechanical equilibrium through a backward Euler integration, residual stresses on elements are released. The configuration may change due to cell division or a change in target growth before the next growth step.

In principle, cells divide when they reach a threshold area, which is twice their initial area and differs by cell type (see Table: Overview of initial and final cell dimensions). The new cell wall is then inserted perpendicular to the cells longest axis, and the existing triangulation is discarded and a new refinement triangulation is created in each of the daughter cells, maintaining the quality of the finite element mesh. As residual stresses are released before division, this replacement causes no change in the force distribution in the tissue. In the particular case of the simulations show in this manuscript, the timeline of simulations is shorter than the period needed for the first cell divisions to occur, hence no divisions are observed.

Tissue layout and boundary conditions

An idealised 2-dimensional structure of the growing, decapitated root was built using MorphoDynamX. In agreement with experimental data, the initial tissue layout has a blunt end and lacks a Quiescent Center (QC), lateral root cap (LRC) and columella, while still displaying the typical cell files of the *Arabidopsis* root (Figure 4A). Our layout simulates only the part of the root directly proximal to the cut side. Within this simulated tissue part, only the cells less than 130μm from the cut were assumed to undergo growth and division, while the other part was assumed to be quiescent (dark coloured cells in Figure 4A). Additionally, we incorporated the experimental observation that during wounding the peptide CLE41 is expressed in cells closest to the cut, resulting in strongly reduced[72] To prevent transmission of forces that result in shape changes at the proximal end of the simulated tissue, Dirichlet boundaries were imposed on all other boundaries of the tissue (Figure 4A, red lines).

Tissue growth was simulated from 0 to 19 hpc. This enabled us to determine cell shapes, skewedness angles and cell axis orientation in the same time window as done for experimental observations.

Growth rate differences in the MorphoMechanX

To investigate the hypothesis that growth rate differences between different cell files lead to the formation of rhomboid cells, we simulated experimentally observed growth rate differences as well as alternative scenarios to investigate the importance of growth rate difference in different cell layers. Growth rates applied in the different simulations are given in Table: Overview of growth relative growth rates used in different simulations, rates are given relative to the endodermal growth rate of 0.05 μm per μm of tissue per hour. Growth rates were calculated based on observations of change in cell sizes between 7hpc and 17 hpc in the regenerating root tip.

Note that instead of taking over the experimentally measured growth rate differences per individual cell file in our model, we only distinguish epidermal, cortical+endodermal, and general vasculature growth rates and use rounded off numbers for growth rate differences. The reasons for this approach are two-fold. First, the aim of our model is to demonstrate that with limited ingredients experimental observations can be qualitatively explained hence showing that these ingredients are necessary and sufficient to explain the phenomenon, not that we can fit a large range of details in a model to quantitative match the experimental observations. Secondly, it is important to realize that the experimentally measured growth rates are resultant growth rates, i.e. not the growth rates following from the individual cells regulatory states but the growth rates that emerged on the tissue scale from their individual growth rates and those of their neighbors. In contrast, the growth rates we impose in our model are applied to the different cells, and not the resultant growth rates.

Table. Overview of growth relative growth rates used in different simulations.

Model	Epidermis Growth Rate	Cortex-Endodermis Growth Rate	Vasculature Growth rate
Uniform Growth	1	1	1
Fast Vasc	1	1	1.5
Slow Epi	8	1	1
Fast Vasc & Slow Epi	8	1	1.5

Cell sizes in the MorphoMechanX

We started our simulations with cell sizes that were based on experimental data. To investigate whether cell sizes have an effect on the extent of formation of rhomboid cells and the development of cellular axes we also investigated an alternative mesh making use of alternative cell sizes. Specifically, we investigated the consequences of cortical cells having a shorter and wider shape. Default and alternative cell dimensions are shown in Table: Overview of initial and final cell dimensions.

Table. Overview of initial and final cell dimensions.

	Default model dimensions		Alternative model dimensions	
Cell types	Height (μm)	Width (μm)	Height (μm)	Width (μm)
Epidermis	10	18	8	18
Cortex	10	12	8	20
Endodermis	12	8	8	12
Pericycle	14	6	8	8
Vasculature	14	5	8	6

Measuring of skewing angle from the MorphoMechanX based FEM simulations

To compare emerging cell shapes in the model to experimental observations of rhomboid cell generation, we measured in our simulations the simulated the angle of the upper and lower cell walls against the vertical plane; which in the experimental measurements were referred to as gamma and epsilon, respectively. This was performed through manual analysis (using an electronic protractor) of images generated from the end of the simulation representing the tissue state at ~19hpc.

Measuring of cell axis orientation from the MorphoMechanX based FEM simulations

The experimental results show a changing angle of newly dividing cell walls as observed cell shapes change, which we could reproduce in our simulations when incorporating growth rate differences. A 3D single cell models of cortical microtubule arrays known to drive division orientation (Figure 6) predicts that the resulting shape change into a rhomboidal cell drives this division and growth reorientation. To investigate if growth rate differences are sufficient to create the level of rhomboidness necessary to induce these division orientation changes, we need to incorporate into our 2D multicellular model a measure of the internal geometry and axial orientation of individual cells. We do so by utilizing the familiar technique of principal component analysis, applied to the coordinate points of the triangulation nodes within a cell. The coordinates of each of these points is in 2D, they are a way to establish an orthonormal basis for each individual cell, such that their major and minor diagonal can be estimated for 2 dimensions.

Simulation for Microtubule based prediction of diagonal division in rhomboid cells

The plant cortical microtubules (MTs) are confined to a thin layer of cytoplasm just inside the plasma membrane, known as the cell cortex. Two-dimensional attachment to the cell cortex allows MTs to interact with each other via collisions. Depending on the value of the collision angle, three key events are observed[73]: For shallow angles (≤ 40), a growing MT bends toward the direction of the MT encountered, and such an adaptive event is called zippering. For steeper angles (≥ 40), the encounter may lead to an induced catastrophe, where the initially growing MT switches to a shrinking state. Alternatively, the growing MT may slip over the one encountered, an event known as crossover (Figure S5A). Plant cells have well-defined, relatively flat faces often connected at sharp edges of significantly higher curvature. MTs, when encountering these edges, undergo additional catastrophes with a probability that increases with increasing curvature of the cell edge.[74] This type of catastrophe originating from the curvature at the cell edge is known as edge catastrophe. To implement edge catastrophe in our simulations, we followed a previous approach,[59] where the curvature effect was captured through the angle (θ) between the adjacent cell faces. In our simulations, the probability of edge catastrophe was calculated using the formula, $Ecat = 1/2(1 + \cos\theta)$. This implementation ensures that Ecat increases as the θ decreases, i.e., higher edge catastrophe for shallow edge angle (Figure S5A). To obtain appropriate MT dynamic parameters, again, we used a previous definition of the control parameter (G),[75] which encapsulates six different MT dynamics parameters, namely growing speed (v_+), shrinking speed (v_-) and treadmilling speed (v^{tm}), induced catastrophe rate (r_c), rescue rate (r_r), and nucleation rate (r_n) and of the following form:

$$G = -\frac{l_0}{l_{avg}} = \left(\frac{2(v_+ - v^{tm})(v_- + v^{tm})}{r_n(v_+ + v_-)}\right)^{1/3} \Bigg/ \left(\frac{r_r}{(v_- + v^{tm})} - \frac{r_c}{v_+ - v^{tm}}\right)^{-1}$$

Here, l_0 is the MT-MT interaction length, and l_{avg} is the average length of MTs without interaction effects. To get the suitable set of parameters that guarantees the steady-state formation of an ordered MT array, we performed simulations on a sphere surface with an area equal to the area of experimentally obtained rhomboid cell surfaces. These simulations were performed until a steady was achieved, where we independently varied l_0 (by varying r_n) and l_{avg} (by varying r_c) while taking the remaining parameters from Deinum et al.[76] In all our simulations, we considered a finite tubulin pool to speed up the relaxation towards a steady.

Deconvolution and Analysis of orientation of microtubules

Deconvolution of the multiphoton images of MBD was done using Huygens Professional v16.1 software. Deconvolution of the images was done at average background value detected automatically by the software using the In/near object estimation mode (area

radius= 0.4μm), maximum number of iterations =60, signal – to – noise ratio (SNR) 13.95 and quality change threshold was set to default value of 0.01. Acuity was set at 20 sharper and the iteration mode was the default 'Optimized'. The point spread function (PSF) values used were automatically generated theoretical PSF by the software. Deconvoluted images were finally exported using TIFF 8bit file with contrast stretch conversion method. Microtubule anisotropy was calculated using the deconvoluted images with the help of FibrilTool ImageJ plugin.[77] For analysing the anisotropy, the ROI was drawn at the cell boundary using the polygonal selection tool. Then the proper channel for fibril and for drawing was selected as described in Boudaoud et al.[77] The tool detected the anisotropy and gave the output in the form a table as well a line in the image showing the principal direction of the orientation of the microtubules.

Statistical analysis

The statistical analysis for regeneration assays and all the quantifications were performed using GraphPad Prism version 10 and Excel 2019 (Microsoft). The statistical tests used for analysis are mentioned in the corresponding figure legends. The median and the individual data points are marked on the graphs representing exterior deformation angle, and the normalized growth rates. For the rest of the graphs, the Mean ± SEM is shown. Fisher's exact test was used for regeneration efficiency. Mann-Whitney test or Unpaired t-test were used for quantification of number of diagonally dividing cells and rhomboidal cells. Paired t-test was computed for the quantification of angle of tapering (θ). The statistics for exterior angles, normalized growth rate quantifications were performed using Kruskal Wallis test ($\alpha = 0.05$) or ANOVA. Normality test for the data was done using the D'Agostino-Pearson test. The significance values are defined as follows: *$p<0.05$, **$p<0.01$, ***$p<0.001$ and ****$p<0.0001$.